Article

Construction of Highly Efficient $Zn_{0.4}Cd_{0.6}S$ and Cobalt Antimony Oxide Heterojunction Composites for Visible-Light-Driven Photocatalytic Hydrogen Evolution and Pollutant Degradation

Chen Chen [1,*] , **Xiao Zhang [2,3]** , **Ting Cheng [2]** , **Mingyue Wen [1]** , **Yuan Tian [1]** and **Baoxuan Hou [1]**

[1] School of Environmental and Chemical Engineering, Jiangsu University of Science and Technology, Zhenjiang 212100, China
[2] School of Environmental Ecology, Jiangsu City Vocational College, Nanjing 210017, China
[3] Yancheng Academy of Environmental Technology and Engineering, Nanjing University, Yancheng 224000, China
* Correspondence: chenc@just.edu.cn

Abstract: Photocatalytic technology could effectively degrade pollutants and release hydrogen. Herein, novel composite materials of $Zn_{0.4}Cd_{0.6}S$ (ZCS) and cobalt antimony oxide (CSO) with different proportions were successfully synthesized through a hydrothermal reaction process. It was proved via various characterization analyses that abundant nano ZCS particles (about 100 nm) were closely coated on the surface of larger CSO particles in the composite photocatalysts, and the heterojunction structure was formed. The synthesized materials could be used as highly efficient photocatalysts to boost the photocatalytic hydrogen evolution and degradation of methylene blue (MB) in visible light. The composite photocatalysts displayed favorable stability, and the optimal proportion was ZCS/1CSO. In addition, the composite materials exhibited a wider absorption range for visible light, and the apparent hydrogen production rate was about 3.087 mmol·g^{-1}·h^{-1}. Meanwhile, compared with single materials, the composite photocatalyst obtained higher photocurrent response and lower electrochemical impedance through conducting photo-electrochemical experiments and analysis. Moreover, all of the photo-generated electrons, superoxide radicals, photo-generated holes, and hydroxyl radicals were proved to contribute the MB photodegradation and hydrogen evolution, and the former two active species played more vital roles. Furthermore, the effective separation of photo-generated electrons and holes through the n-type of ZCS and p-type of CSO heterojunction structure accelerated the improvement of photocatalytic abilities for composite materials. The photo-generated electrons concentrated in the conduction band of ZCS might be helpful for the improvement of hydrogen evolution abilities of composite photocatalysts. This work not only provides a novel strategy towards high-efficiency composite photocatalysts through constructing heterojunction assisted with hydrothermal reaction, but also demonstrates the possibility of utilizing binary composites for enhanced hydrogen evolution reaction and pollutant degradation.

Keywords: cobalt antimony oxide; ZnCdS; photocatalytic; hydrogen evolution; pollutant degradation

1. Introduction

As we know, critical organic wastewater pollution has resulted from the rapid increase in chemical production and development [1–4]. Wastewater discharged without treatment will have a significant impact on ecological environment and human health [5–8], inducing cancer [9,10], mutagenicity [11,12], teratogenicity [13,14], water eutrophication [15,16], etc. The pollution will reduce the quality of environmental water, thus making it unable to be directly applied in drinking and other industrial fields [17–19]. Therefore, the efficient treatment technology of organic wastewater has always been the focus of wastewater

treatment research. At the same time, in order to fundamentally reduce the amount of pollution, people are also looking for ways to obtain new, clean energy. The hydrogen-based energy is one of the research focuses [20].

Photocatalysis, as a promising strategy for its photodegradation of organic wastewater and hydrogen evolution capacity [21], has been widely investigated because of its ambient operating temperature and pressure, high efficiencies, environment-friendly, and low operating costs. It was reported that photocatalysts play a crucial part in the photogradation of pollutants. Photocatalysts could produce the photo-generated electrons and photo-generated holes that participate in the process of oxidation and reduction reaction, and then accelerate the degradation of various pollutants, including organic substances. Hence, as one of the vital factors in photocatalysis technology, developing highly efficient photocatalysts have been attracted more attention from researchers in related fields.

The photocatalytic technology applies light to excite photocatalysts, so as to produce free radicals and efficiently degrade pollutants [22,23] and hydrogen evolution [24]. Generally, the photocatalytic reaction takes advantage of semiconductor materials as the photocatalyst. According to the classical solid energy band theory, when the excitation light energy was higher than the energy bandwidth of the photocatalyst, electrons would be excited from the valence to the conduction band to form free electrons, and free holes would be left in the valence band. The free electrons and holes could directly react with pollutants by themselves, or form superoxide radicals and hydroxyl radicals to degrade pollutants [25,26]. In addition, different from other wastewater treatment technologies, due to its strong reactivity, the photocatalytic technology generated free radicals can not only degrade pollutants but also reduce H_2O molecules to obtain hydrogen [27,28]. Hence, the development of photocatalytic technology could not only effectively deal with organic water pollution, but also provide a new direction for new clean energy. From this point of view, photocatalysis is a promising solution for the current environmental problems and energy crisis, which can capture the large scale of solar energy and deliver an alternative energy carrier to chemical energy.

Similar to other catalytic technologies, the highly efficient photocatalyst plays a key role in the process of photocatalyst reaction. Since the initial TiO_2 [29,30], a large number of materials have been proven photocatalytic abilities, including C_3N_4 [31,32], ZnO [33,34], MoS_2 [35,36], $ZrMo_2O_8$ [37,38], Ag_3PO_4 [39,40], $AgSbO_3$ [41], $Zn_xCd_{1-x}S$ [42,43], etc., and some new photocatalytic materials are developed every year. However, challenges are still to be overcome to achieve viable photocatalysts for practical application. Researchers attempted to improve the abilities to absorb a wide range of the solar spectrum, suppress the recombination of photo-generated electrons and photo-generated holes, or reduce the bad gap of photocatalysts. Among various photocatalysts, each photocatalytic material displays its own properties. Take $Zn_xCd_{1-x}S$, for example; it has been proven to be an efficient material for the photocatalytic degradation of pollutants and hydrogen evolution. However, for a single photocatalytic material, the recombination of photo-generated electrons and holes was one of the key factors limiting the improvement of photocatalytic efficiency, and $Zn_xCd_{1-x}S$ is not an exception. In order to solve the recombination problem, constructing a binary or a ternary composite heterojunction is considered an effective way. The transfer of photogenerated electrons and holes between the conduction and valence band of binary and ternary heterojunction can greatly reduce the recombination probability of electrons and holes, thus improving pollutant degradation and photocatalytic hydrogen evolution performance [24]. Madhusudan constructed a highly efficient $Zn_xCd_{1-x}S/Au@g-C_3N_4$ ternary heterojunction composite and obtained higher visible light catalytic efficiencies [43]. Shen et al. synthesized low-cost Ni_3C/twin-crystal $Zn_{0.5}Cd_{0.5}S$ heterojunction/homojunction nanohybrids and gained efficient photocatalytic H_2 evolution ability [44]. Ge et al. developed Cu_3P and decorated $Zn_{0.5}Cd_{0.5}S$ materials for enhanced photocatalytic hydrogen evolution under visible light [45]. The $CeVO_4/Zn_{0.5}Cd_{0.5}S$ heterojunction was prepared by Liu et al. for efficient photocatalytic hydrogen evolution [46]. Qi et al. constructed a $WS_2/Zn_{0.5}Cd_{0.5}S$ nano heterostructured material that exhibited efficient visible light

catalytic performance [47]. So far, new composite photocatalysts with extraordinary photocatalytic properties are still required to develop, and the deeply photodegradation mechanisms in the process of photocatalytic reaction remained to be revealed.

In this work, novel composite materials of $Zn_{0.4}Cd_{0.6}S$ (ZCS) and cobalt antimony oxide (CSO) with different ratios were successfully synthesized through a hydrothermal synthesis reaction. The synthetic products were comprehensively characterized and measured by various advanced techniques, including X-ray diffraction (XRD), scanning electron microscopy-energy dispersive spectroscopy (SEM-EDX), UV–vis diffuse reflectance spectra (UV-vis DRS), and X-ray photoelectron spectroscopy (XPS). On this basis, the photocatalytic degradation of methylene blue (MB) and hydrogen evolution experiments were conducted, and the photocatalytic stability was also analyzed and evaluated. Furthermore, the photo-electrochemical analysis, containing electrochemical impedance spectroscopy (EIS), electrochemical photocurrent, Mott–Schottky curves, and free radical detection were utilized to reveal the photocatalytic mechanism of composite photocatalysts. The findings proved that the binary composite photocatalysts displayed a wider absorption range for visible light, excellent photocatalytic activities for boosting photocatalytic hydrogen evolution, and efficient photodegradation of MB in visible light. Moreover, the photocatalysts exhibited extraordinary stability in the photocatalytic reaction process. Furthermore, the effective separation of photo-generated electrons and holes through the n-type of ZCS and the p-type of CSO heterojunction structures accelerated the improvement of photocatalytic abilities for composite materials. This work not only provides a novel strategy towards highly efficient composite photocatalysts through constructing the heterojunction by hydrothermal synthesis method, but also proves the possibility of using binary composite photocatalysts to enhance the hydrogen evolution abilities and pollutant degradation efficiencies.

2. Materials and Methods

2.1. Catalyst Materials Synthesis Process

All the chemical reagents (analytically pure) were purchased from the Sigma reagent company (Shanghai, China). The synthesis method of each related material can be seen below. The preparation of the cobalt antimony oxide (CSO) sample was as follows: First, 0.005 mol of $NaSbO_3 \cdot 3H_2O$ was dispersed in 80 mL of deionized water, and continued to be stirred for 1 h until a white opaque liquid was formed. Secondly, 0.010 mol of $Co(NO_3)_2 \cdot 6H_2O$ was added to the above white liquid, and the liquid gradually turned reddish brown with flocs. After that, the mixture continued to be stirred for 2 h at a temperature of 50 °C. Third, the mixture obtained in the second step was transferred to a 100 mL Teflon-lined stainless-steel autoclave for hydrothermal reaction. The reaction temperature was 120 °C and the time was 12 h. Finally, the reaction product obtained was cooled, filtered, and rinsed with deionized water, and then transferred to the blast drying oven (LICHEN Technology, Shanghai, China) (at 75 °C) to be dried to a constant weight.

The preparation of the $Zn_{0.4}Cd_{0.6}S$ sample was as follows: First, 0.84 g of Cadmium acetate and 0.45 g of Zinc acetate were added into 70 mL of deionized water, and then stirred for 45 min with the ultrasonic. After that, 12 g of Thiourea was added into the above solution, and then stirred for another 60 min, also with the ultrasound. Secondly, the mixture was transferred to 100 mL of Teflon-lined stainless-steel autoclaves for the hydrothermal reaction. The reaction temperature was fixed at 150 °C and the time was 5 h. Finally, the reaction product was cooled, filtered, and rinsed with deionized water, and then transferred to the blast drying oven (at a temperature of 75 °C) to be dried to a constant weight.

The preparation of composite photocatalytic materials was as follows: First, the CSO material was synthesized according to the above procedures. Then, the synthesized CSO sample was added to 70 mL of deionized water and mixed with 0.84 g of Cadmium acetate and 0.45 g of Zinc acetate at the same time. To obtain different proportions of composites, the dosages of CSO ranged from 0.25 g to 1 g. The subsequent reaction processes were

the same as that of $Zn_{0.4}Cd_{0.6}S$. In addition, the composite photocatalytic materials were recorded as ZCS@xCSO, and the x (unit in g) was the dosage of the added CSO sample.

2.2. Materials Characterization and Mechanism Analysis

To illustrate the various properties of synthesized photocatalytic materials, photocatalysts were characterized by many modern instruments, mainly containing X-ray diffraction (XRD), UV–vis diffuse reflectance spectra (DRS), scanning electron microscopy-energy dispersive spectroscopy (SEM-EDX), and X-ray photoelectron spectroscopy (XPS). The detailed information of instruments was as follows: a HITACHI (Regulus 8100) scanning electron microscope with Super-X EDS detector (HITACHI, Tokyo, Japan) was used to observe the morphologies of catalytic products; a PerkinElmer Ultraviolet spectrophotometer (Shanghai, China) measured the UV–vis DRS spectra; a Shimadzu XD-3A diffractometer (Puxi, Beijing, China) was used to measure the XRD patterns of powder samples, and utilizing the radiation of Cu-Kα (λ = 1.54056 Å); and a PHI 5000 VersaProbe XPS (Thermo Kalpha, USA) was utilized to examine the X-ray photoelectron spectroscopy spectra.

The photocatalysis mechanism was analyzed by photo-electrochemical analysis and the detection of free radicals. The photo-electrochemical properties of materials were analyzed by a CHI 660E electrochemical workstation (Shanghai Chenhua, Shanghai, China). The three electrodes system was used in the electrochemical measurement. The sample electrode was the working electrode, the platinum sheet electrode was the counter electrode, and the saturated calomel electrode was the reference electrode. Additionally, 0.2 mol/L of the Na_2SO_4 solution was the electrochemical test electrolyte. Moreover, the analysis items included electrochemical impedance spectroscopy (EIS), electrochemical photocurrent (the interval was 20 s), and Mott–Schottky curves. The free radicals in the photocatalytic reaction process were analyzed via an electron paramagnetic resonance spectrometer (ESR: EMXmicro-6/1/P/L, Karlsruhe, Germany). Furthermore, the capturing agent for active species ($O_2{}^-$ and OH) was 5,5-dimethyl-1-pyrroline N-oxide (DMPO), and the capturing agent for photo-generated e$^-$ and h$^+$ was 2,2,6,6-Tetramethyl-1-piperidinyloxy (TEMPO).

2.3. Photocatalytic Experiments

The photocatalytic experiments were conducted under visible light irradiation (300 W Xe-lamp, Zhengxin instrument, Yancheng, China). MB was used as the target pollutant to evaluate the photocatalytic degradation activities, and the concentration of MB was 10 mg/L. In each experiment, the photocatalytic material was added to 30 mL of MB solution and the dosage was 0.02 g. Additionally, the reaction mixture liquids were put into a transparent photoreaction vessel and all the photocatalytic degradation tests were conducted at room temperature (25 °C). Prior to the photocatalytic reaction, the mixture was stirred for several minutes in the dark to achieve a sorption-desorption equilibrium, thus the photocatalytic reaction time was set ranged from -10 to 40 min in our experiments, and the light was turned on at 0 min. After the photocatalytic experiments were completed, the residual concentration of MB was determined via an ultraviolet visible spectrophotometer. To evaluate the photocatalytic stability, consecutive experiments were conducted through the reuse of photocatalysts. The photocatalyst solid was recovered by centrifugation with a low-speed centrifuge (LICHEN Technology, Shanghai, China) and washed five times with deionized water. Afterward, the recycled solid was dried in a blast drying oven at a temperature of 75 °C until its weight was constant for the next usage. In our research, the photocatalyst was reused four times. In addition, to investigate the photocatalytic degradation mechanisms, the generation of reactive species was examined through the addition of scavenging chemicals during the photocatalytic reaction process. The trapping chemicals for holes, hydroxyl radical, superoxide free radical, and electron trappers were 0.037 g EDTA-2Na, 0.0094 g TBA (tert-butyl alcohol), 0.0108 g BQ (1,4-benzoquinone), and 0.0142 g CCl$_4$, respectively.

The photocatalytic hydrogen production experiments utilized the Porfila photocatalytic system and a CEL_HXF300/CEL-HXUV300 (Bofeilai, Beijing, China) light source.

The specific reaction steps were as follows: There was 50 mg of photocatalyst material added to a 100 mL aqueous solution of lactic acid (10 wt%), and a chloroplatinic acid solution with a 1% mass ratio was added and mixed, sonicated for 30 min, and then the mixture was transferred to the reaction flask. After that, the reaction flask was placed in the atmosphere controller, using argon to remove the air in the bottle, and was then vacuumed for 1 h. Then, putting the flask in a multi-channel photocatalytic reaction device, and then irradiated for 4 h with a 300 W Xenon lamp. The gas produced was monitored online by a gas chromatograph and the detector was a TCD (Sanfeng, Guangzhou, Guangdong, China) thermal conductivity detector, and the carrier gas was high-purity argon.

3. Results and Discussions

3.1. XRD

The XRD technology can help us better understand the mineral phase composition of materials. Figure 1 depicted the XRD patterns of the $Zn_{0.4}Cd_{0.6}S$/1 g of cobalt antimony oxide (ZCS/1CSO) composite photocatalyst, and the XRD patterns of ZCS and CSO were also detected as a comparison. It could be seen that the main XRD peaks of CSO were located at 2θ (crystal facet): 14.8° (111), 28.5° (311), 30.1° (222), 34.5° (400), 37.9° (331), 45.7° (511), 50.0° (440), 52.4° (531), 59.2° (622), 62.1° (444), and 64.3° (711). Meanwhile, the main XRD peaks of ZCS were located at 2θ: 25.5 (100), 27.1 (002), 28.7° (101), 44.4° (110), 47.2° (103), and 52.8° (112). In addition, both the XRD peaks of CSO and ZCS could be observed in the pattern of ZCS/1CSO. Additionally, as the proportion of CSO mass increased, the relative intensities of its XRD peaks gradually increased (Figure S1). This finding indicated that ZCS/CSO might be a complex of ZCS and CSO. This is the premise for composite materials to become a binary heterostructure.
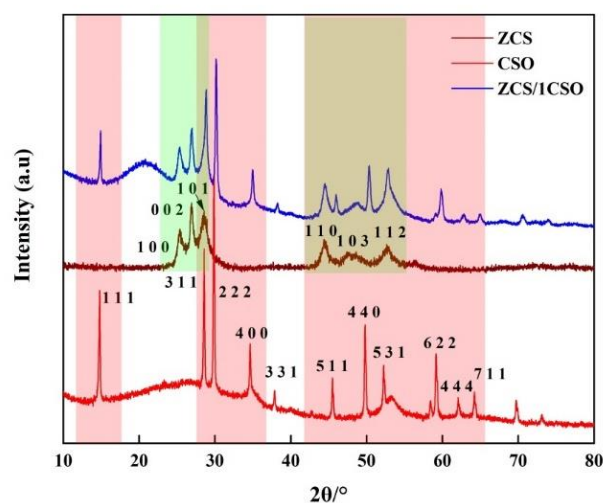

Figure 1. XRD patterns of ZCS, CSO, and ZCS/1CSO compound.

3.2. UV–Vis DRS

The UV–vis DRS technology could well show the absorption efficiency of solid semiconductor materials to different frequencies of light, and calculate the band gap. Figure 2 showed the UV–vis diffuse reflectance spectra for ZCS, CSO, and ZCS/1CSO compounds. It could be observed in Figure 2 that ZCS material displayed superior absorption for visible light less than 500 nm wavelength, which was consistent with the results of the relevant literature. At the same time, the light absorption range of the CSO catalytic material was slightly wider than that of the ZCS material, and it could absorb a wavelength of light less than 700 nm. After the materials underwent a composite reaction, the visible light absorption range of the ZCS/1CSO catalytic material had greatly expanded. The ZCS/1CSO composite photocatalyst displayed excellent visible light absorption for the wavelength below 850 nm. Similar findings could also be found in the results of compounds with

different mass ratios (Figure S2). As depicted in Figure S2a, when the adding the mass of CSO, the synthetic process increased from 0.25 g to 1 g, and the light absorption capacities (lower than 850 nm) of composites were gradually improved. Then, after the added mass of CSO, it continued increasing to 1.5 g, and the light absorption capacities decreased gradually. This result suggested that there existed a relatively appropriate ratio between CSO and ZCS for the performance of light absorption. Hence, from the perspective of light absorption, 1 g dosage of CSO in a synthetic process might be the best value of the ratio between CSO and ZCS. Moreover, the Tauc equation was usually used to estimate the band gap value based on UV–vis DRS data [48,49], the intercept between the straight line part in the hv and $(\alpha hv)^2$ relation curve of Figure 2b and the *x*-axis should be the band gap value of the sample. In Figure 2b, it could be seen that the band gap of the ZCS sample should be 2.45 eV, which was similar to references [50,51]. Meanwhile, the band gap of CSO was about 2.0 eV, and such a value was consistent with its absorption ability for visible light below a wavelength of 700 nm. For compound photocatalytic materials, it should be difficult to calculate a single band gap value. In the fitting result of ZCS/1CSO, it could be obviously found that there were two direct parts with an intercept of 1.41 eV and 2.39 eV, respectively. These similar results could be observed in the fitting curves of samples with different mass ratios (Figure S2b). This result implied that, through the composite reaction process, the band gap of composite materials was reduced, which greatly enhanced the light absorption range and intensity. This made the composite material could use light energy more efficiently, and then generate more photogenerated electrons and holes.
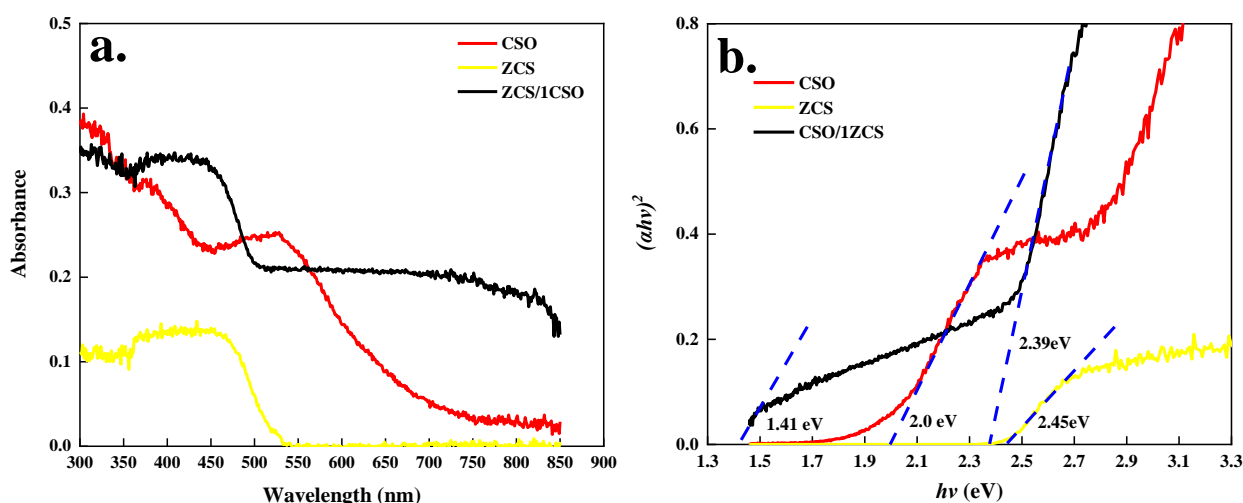

Figure 2. UV–vis diffuse reflectance spectra for ZCS, CSO, and ZCS/1CSO compounds (**a**), and the plotting results of band gaps energy for ZCS, CSO, and ZCS/1CSO compounds (**b**), the blue line presents the straight line part (in the hv and $(\alpha hv)^2$ relation curve.

3.3. SEM-EDX

The SEM-EDX technology can help us better understand the micromorphology and composition of materials. Figure 3 showed the SEM analysis results of CSO. In Figure 3a,b, it could be seen that the original CSO clearly presented the hexahedron morphology and the side length was about 5 μm. From the element mapping results (Figure 3b–d), the elements of Co, Sb, and O were uniformly distributed around all the particle area in Figure 4a. Therefore, the main constituent elements of CSO were Co, Sb, and O, and the atom ratio was 1:2:10, which meant that the CSO particle was cobalt antimony oxide. Meanwhile, as depicted in Figure S3, plenty of nano rough sphere particles could be clearly observed, and the particle size was about 100 nm. According to the element mapping results (Figure S3c–e), the main constituent elements of ZCS were Zn, Cd, and S, and the atom ratio was 0.4:0.6:1. Such morphology of nano rough spheres had also been found by other researchers [43]. This nanostructure allowed ZCS to absorb light more efficiently.
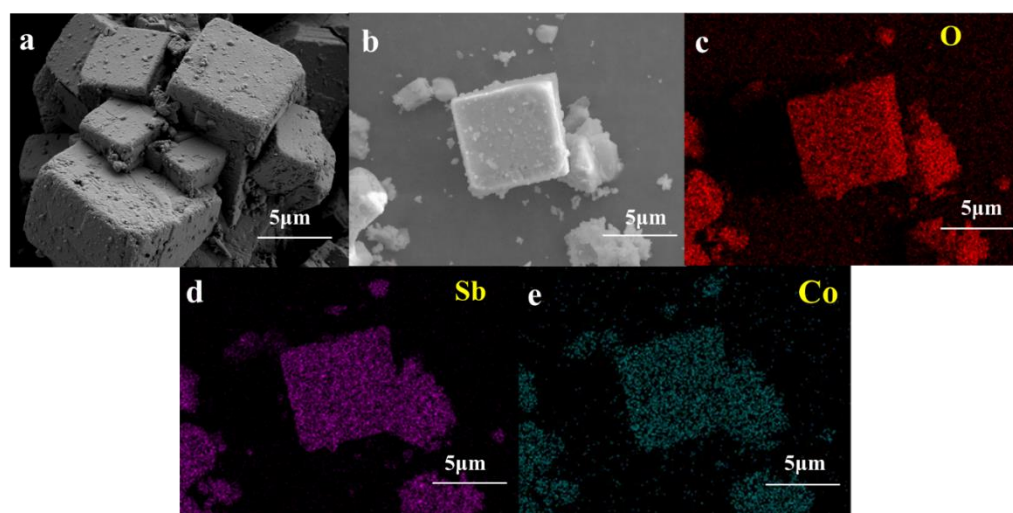
Figure 3. The SEM analysis results of CSO (**a**,**b**) and EDS mapping results of O (**c**), Sb (**d**), and Co (**e**).
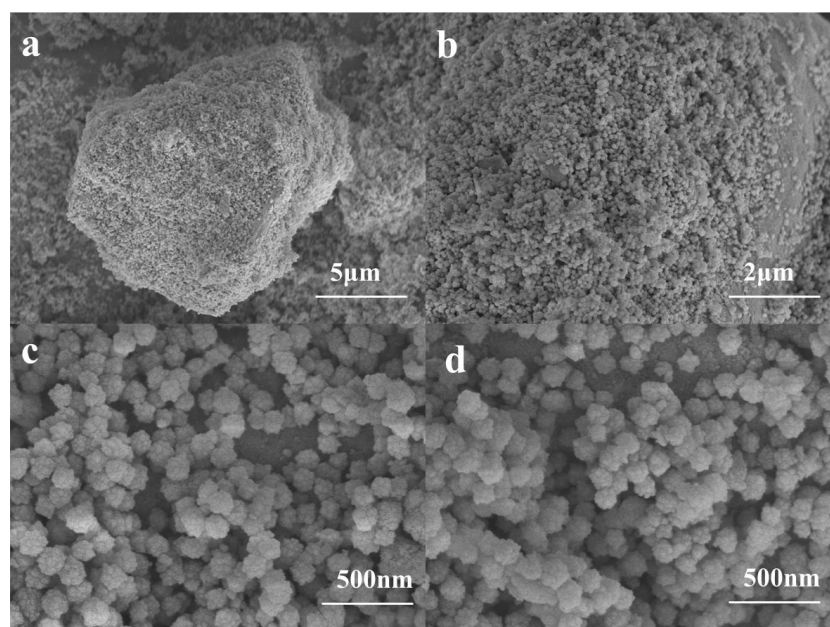

Figure 4. SEM analysis results of the ZCS/1CSO sample, the overall morphology of particles (**a**), the particle surface morphology (**b**), the micro details of particle surface (**c**,**d**).

Figure 4 described the SEM analysis results of the ZCS/1CSO photocatalyst. It could be seen in Figure 4a,b that after the compound reaction, the hexahedron particle became irregular and the particle size was also about 5 μm. Moreover, in Figure 4b–d, it could be observed that the surface of the irregular particle was covered by a large amount of nano spheroid-like particles. These nanoparticles have a similar morphology to Figure S3. As we know, Figure S3 presented the morphology of the original ZCS, thus the same nano spheroid-like particles found in Figure 4 should also be the ZCS particles. Obviously, this close contact was conducive to the transfer of photogenerated electrons and holes between ZCS and CSO. Figure 5 presented the EDS mapping results of the ZCS@1CSO composite photocatalyst. It could be known that the elements of Zn, Cd, and S are distributed around all the areas of spherical-like particles in Figure 4a. The atom ratio of Zn, Cd, and S was about 0.38:0.62:0.95, which was very close to that of the original ZCS. At the same time, the elements of Co, Sb, and O were much more evenly distributed throughout the regions of Figure 5a. The atom ratio of Co and Sb was about 1:2, which was similar to

that of the original CSO. Furthermore, the more clear analysis results could be obtained from the EDS point and line in Figure 6. The EDS line in Figure 6a was extended across the area of nano spherical-like particles and irregular bigger particles. Additionally, in Figure 6h,i, it was found that the main element composition of nano spherical-like particles (point 1) was Co, Sb, and O, while that of irregular bigger particles (point 2) was Zn, Cd, and S. Meanwhile, in the results of Figure 6b–g, it could be observed that the element composition was changed significantly at 19 μm of the EDS line (the interface between two particles). Near there, it could be found that the content of elements Zn, Cd, and S began to decrease while the content of elements Co, Sb, and O gradually increased. Based on the analysis of the above results, it could be summarized that, after the composite reaction of materials, massive nano ZCS particles were tightly loaded on the surface of CSO particles. After the light excitation, such microstructures of composite photocatalysts would provide excellent contact conditions for the photo-generated electron and hole transfer between the two particles.
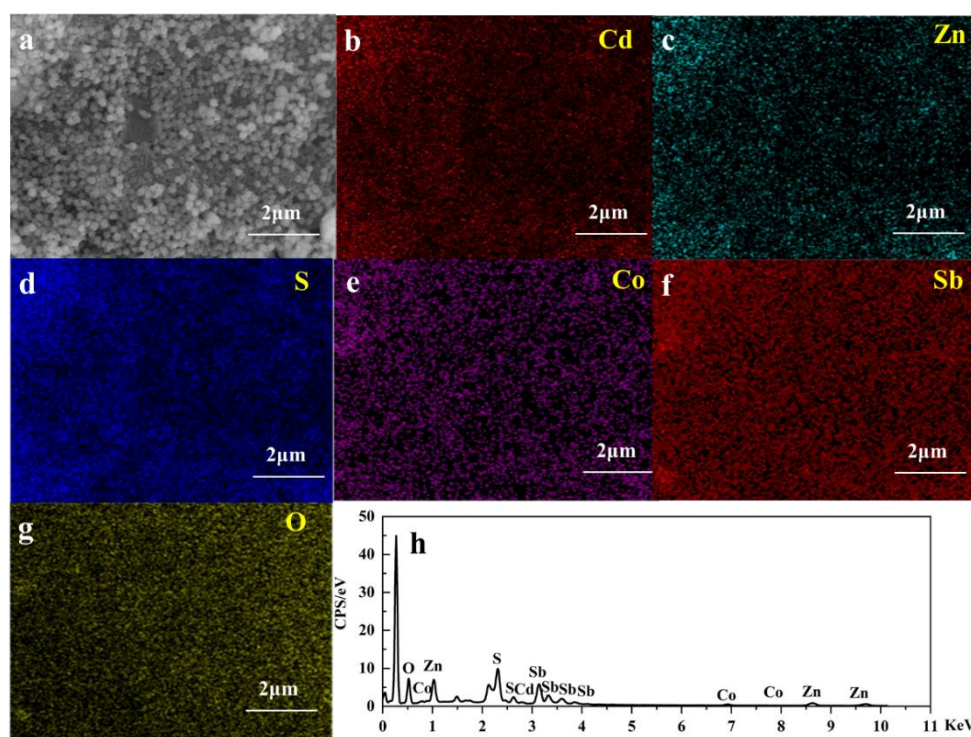

Figure 5. The EDS mapping results of ZCS@1CSO, the analysis area (**a**), Cd (**b**), Zn (**c**), S (**d**), Co (**e**), Sb (**f**), O (**g**), the total element EDX analysis of analysis area (**h**).

3.4. XPS

XPS technology could help us to understand the surface elemental composition and the form of materials. Figure 7 showed the XPS analysis results of the CSO material. In Figure 7a, it could be seen that the main XPS peaks of CSO were located at 975.3 eV (Sb3s), 814.5 eV (Sb2p$_{1/2}$), 795.6 eV (Co2p$_{1/2}$), 783.4 eV (Co2p$_{3/2}$), 768.1 eV (Sb2p$_{3/2}$), 537.0 eV (Sb3d), 530.1 eV (O1s), 154.2 eV (Sb4s), 103.9 eV (Co3s/Sb4p), 59.3 eV (Co3p), and 36.8 eV (Sb4d). All these elements were the constituent elements of CSO, and that was consistent with SEM-EDS results. Figure 7b,c depicted the high-resolution XPS spectra of Co2p and O1s/Sb3d. Figure 7b suggested that the Co2p peaks could be divided into two main peaks at 782.4 eV (Co2p$_{3/2}$) and 798.4 eV (Co2p$_{1/2}$). In addition to the above two peaks, two satellite peaks, located at 787.6 eV and 803.8 eV, could also be found. The appearance of these four peaks was related to the +2 valence Co element in the CSO material [52]. Meanwhile, in Figure 7c, it also could be seen that the peaks of Sb3d and O1s were partly overlapped. After peak splitting, the Sb3d$_{5/2}$ and Sb3d$_{3/2}$ peaks were at 533.8 eV and

540.8 eV, and the main O1s peak was at 532.3 eV. The appearance of the Sb3d$_{5/2}$ and Sb3d$_{3/2}$ peaks suggested the existence of a +5 valence Sb element in the CSO catalytic material [52,53].
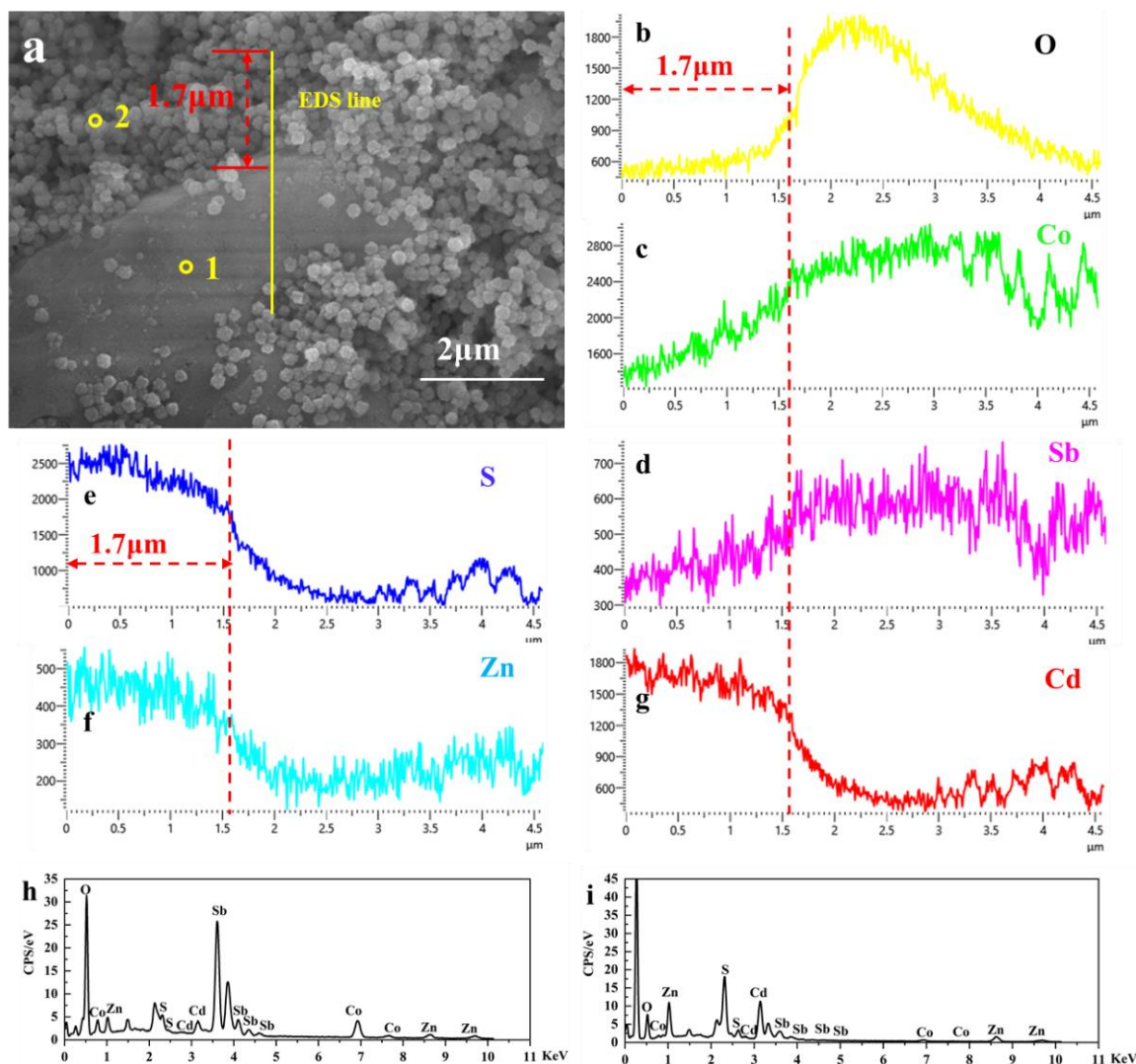

Figure 6. The element distribution along the EDS line in (**a**), ((**b**): O, (**c**): Co, (**d**): Sb, (**e**): S, (**f**): Zn, and (**g**): Cd) and EDS results of point 1 (**h**) and point 2 (**i**) in (**a**).

Moreover, Figure 8 showed the XPS results of the ZCS/1CSO composite photocatalyst. As depicted in Figure 8a, the main XPS peaks of ZCS/1CSO included 1047.9 eV and 1044.4 eV (Zn2p), 974.9 eV (Sb3s), 815.2 eV (Sb2p$_{1/2}$), 797.0 eV (Co2p$_{1/2}$), 784.1 eV (Co2p$_{3/2}$), 769.1 eV (Sb2p$_{3/2}$), 621.1 eV (Cd3p), 537.2 eV (Sb3d), 530.2 eV (O1s), 501.8 eV (Zn LMM), 405.4 eV (Cd3d), 230.1 eV (S2s), 164.1 eV (S2p), 142.7 eV (Zn3s), 89.4 eV (Zn3p), 37.3 eV (Sb4d), and 7.1 eV (Cd4d). The elements appearing in the above XPS peaks covered all the elements contained in the ZCS/1CSO photocatalytic material.
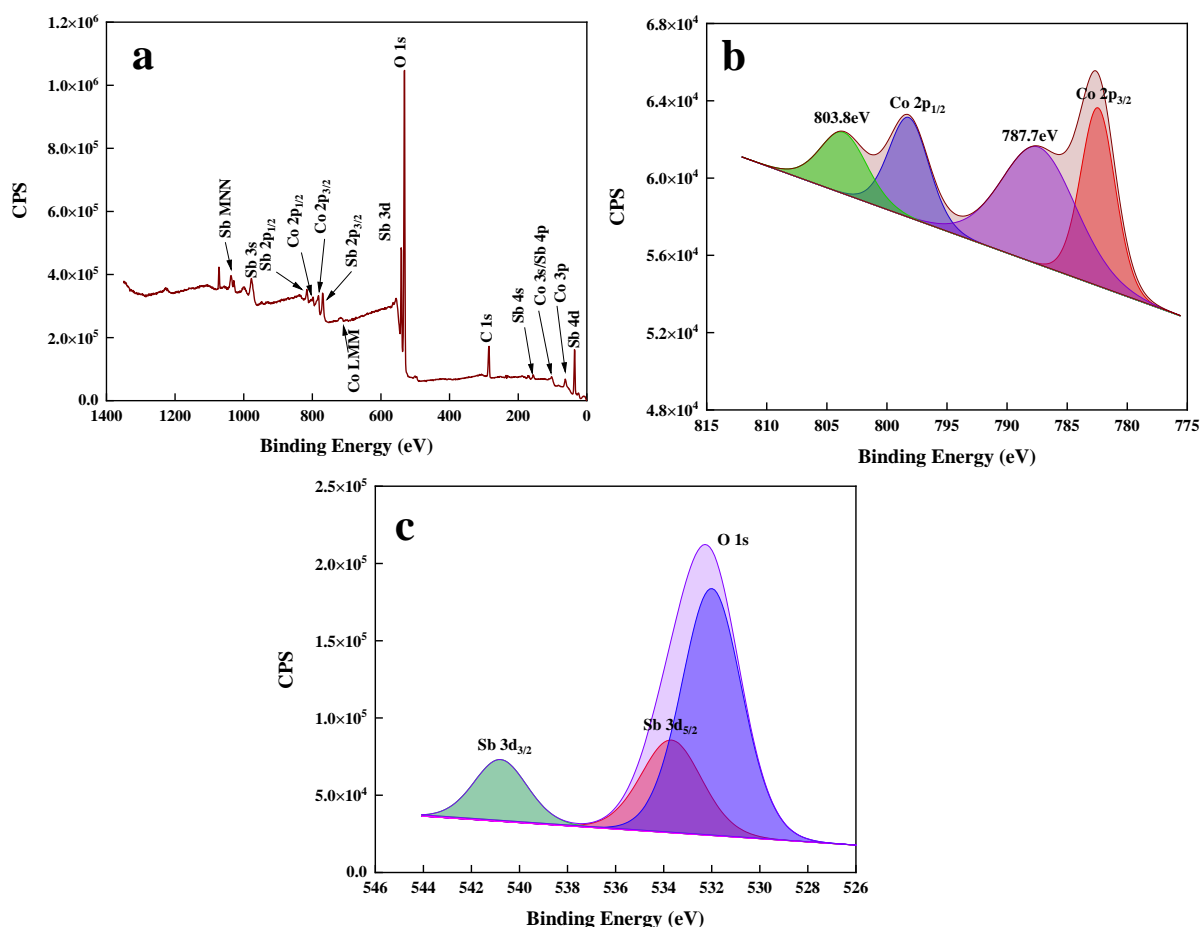
Figure 7. The wide scan XPS of CSO (**a**); the high-resolution XPS spectra of Co2p (**b**) (the green and purple area represented the satellite peaks of Co2p$_{1/2}$ and Co2p$_{3/2}$, the blue and red area represented the main peak of Co2p$_{1/2}$ and Co2p$_{3/2}$; the high-resolution XPS spectra of O1s/Sb3d (**c**) (the light green, light red and light blue area represented the main peak of Sb 3d$_{3/2}$, Sb 3d$_{5/2}$ and O1s).

Furthermore, comparing Figures S4a and 7a with Figure 8a, it was found that all the above peaks (at similar positions) appeared in the XPS results of the original ZCS and CSO material. As depicted from the high-resolution XPS spectra of Cd3d (Figure 8b) and Zn2p (Figure 8c), it could be observed that the XPS peak of Cd3d was split to Cd3d$_{5/2}$ (407.4 eV) and Cd3d$_{3/2}$ (414.2 eV) peaks. Similarly, the XPS peaks of Zn2p were split into Zn2p$_{3/2}$ (1023.9 eV) and Zn2p$_{1/2}$ (1046.8 eV) peaks. The peaks with similar shapes and positions could also be found in the results of the original ZCS material (Figure S4b,c), and the occurrence of Cd3d and Zn2p peak splitting suggested the existence of a +2 valence Cd and the Zn element in ZCS and ZCS/1CSO photocatalysts. Additionally, Figures 8d and S4d indicated the high-resolution XPS spectra of S2p in the ZCS/1CSO and ZCS material. The appearance of S2p was directly related to the −2 valence S element in the two catalytic materials. In Figure 8d, it could be observed that the S2p peaks were composed of two peaks at 164.2 eV and 166.2 eV. A similar appearance also could be observed in Figure S4d, and this peak splitting (close peak position) should be caused by the different energies of the Cd-S bond and Zn-S bond in the ZCS and ZCS/1CSO materials. Additionally, the high-resolution XPS spectra of O1s/Sb3d and Co2p were shown in Figure 8e,f. Compared with Figure 7b,c, the similar peaks splitting and position in Figure 8c,f indicated the elements of Co and Sb keep a +2 and +5 valence in the ZCS/1CSO composite photocatalyst after the compound reactions, respectively. In summary, based on the XPS results, it could be believed that the ZCS/1CSO photocatalyst was a complex of ZCS and CSO materials, which was consistent with other characterization results.
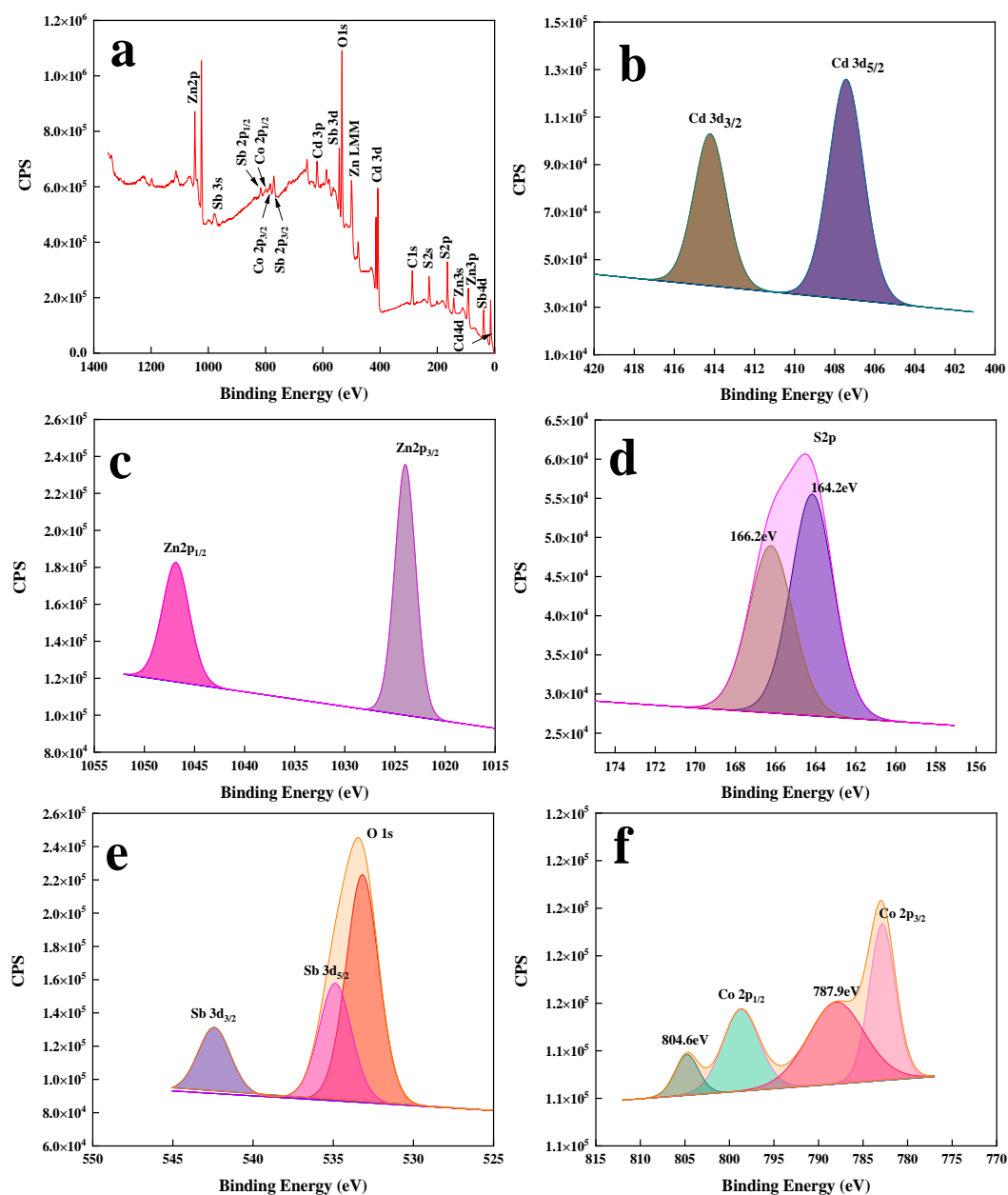
Figure 8. The wide scan XPS of ZCS/1CSO (**a**), the high-resolution XPS spectra of Cd3d (**b**) (the grey and deep purple area represented the main peaks of Cd3d$_{3/2}$ and Cd3d$_{5/2}$), the high-resolution XPS spectra of Zn2p (**c**) (the pink and light purple area represented the main peaks of Zn 2p$_{1/2}$ and Zn 2p$_{3/2}$); the high-resolution XPS spectra of Zn2p (**d**) (the light grey and purple area represented two split peaks of S2p at 166.2 eV and 164.2 eV); the high-resolution XPS spectra of O1s/Sb3d (**e**) (the purple, light red and light orange area represented the main peak of Sb3d$_{3/2}$, Sb3d$_{5/2}$ and O1s); the high-resolution XPS spectra of Co2p (**f**) (the deep green and red area represented the satellite peaks of Co2p$_{1/2}$ and Co2p$_{3/2}$, the light green and light pink area represented the main peak of Co2p$_{1/2}$ and Co2p$_{3/2}$.

3.5. The Photocatalysis Performance

The photocatalytic performance of the materials in this study was tested by both methylene blue degradation and hydrogen evolution. Figure 9a depicted the photocatalytic degradation process of MB under different systems. It was seen that under the conditions of single pure visible light (no catalyst) and single catalyst (no visible light), the degradation efficiencies of MB were very low. While with the combined action of catalyst and

visible light, it was observed that the degradation efficiencies of MB were greatly improved. Additionally, among the three typical degradation systems, the ZCS@1CSO combined system gained the highest degradation efficiencies for the target pollutant. After the photocatalytic reaction was conducted for 40 min, the target pollutant was almost completely degraded. In addition, compared with the photocatalytic degradation efficiencies with different ratios of composite photocatalysts (Figure S5a), the degradation efficiencies of MB with the ZCS@1CSO composite were also the highest among all the other photocatalytic systems. Figures 9b and S5b, and Table 1 display the pseudo-first-order kinetics analysis results of different degradation systems [54,55]. It could be seen that, except for the single pure visible light and single catalyst systems, the fitting values of R^2 in all photocatalytic systems were higher than 0.99. Such findings suggested that the pseudo-first-order kinetic equation could better describe the photocatalytic degradation process of MB in different reaction systems.
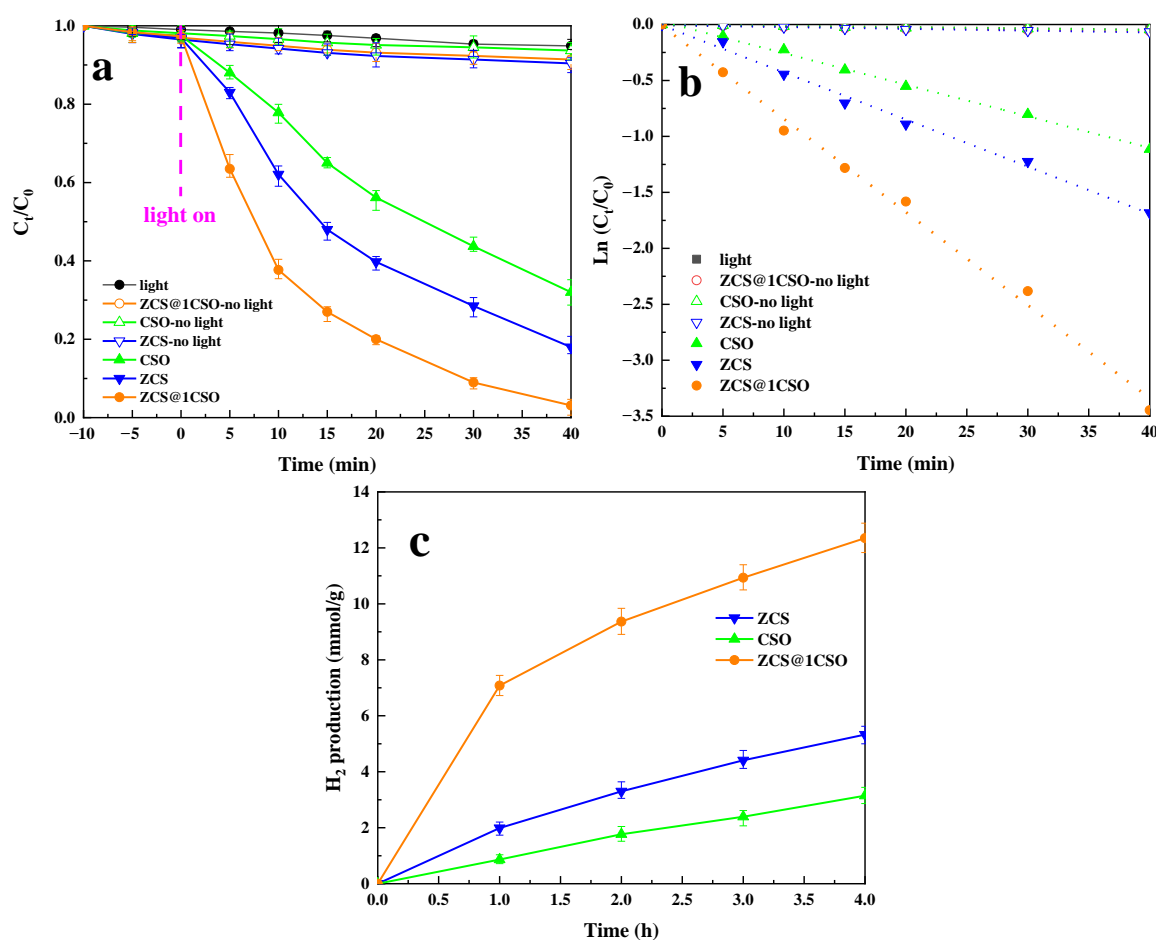

Figure 9. The MB photocatalytic degradation process (**a**), pseudo first order kinetic analysis (**b**) and H_2 production (**c**) under different photocatalytic systems.

In addition to degrading pollutants, suitable photocatalytic materials could also generate hydrogen by splitting water. Figures 9c and S5c, and Table 1 showed the H_2 production results in different photocatalytic systems. The findings indicated all the photocatalytic systems could produce hydrogen and the ZCS@1CSO system acquired the maximum values of hydrogen. Additionally, the highest hydrogen production amount at 4 h was about 12.35 mmol·g^{-1}, and the rate constant of apparent H_2 production was around 3.087 mmol·g^{-1}·h^{-1}. In a word, the related photocatalysis results indicated that the combined usage of ZCS and CSO materials could not only promote the photocatalytic degradation efficiencies of MB, but also greatly improved the hydrogen evolution efficiencies.

Table 1. The photocatalytic kinetic analysis results.

Different Reaction System	MB Degradation Rate Constant	Standard Deviation	R^2	Apparent H_2 Production Rate Constant $(mmol \cdot g^{-1} \cdot h^{-1})$
light	0.00116	0.0000707	0.9780	-
ZCS-no light	0.00161	0.0001387	0.9476	-
CSO-no light	0.00115	0.0001060	0.9509	-
ZCS@1CSO-no light	0.00147	0.0001535	0.9486	-
ZCS	0.0421	0.0006465	0.9931	1.332
CSO	0.0282	0.000143	0.9969	0.787
ZCS@0.25CSO	0.0483	0.000186	0.9912	2.023
ZCS@0.5CSO	0.0544	0.000182	0.9933	2.395
ZCS@0.75CSO	0.0619	0.000223	0.9922	2.861
ZCS@1CSO	0.0832	0.000282	0.9932	3.087
ZCS@1.25CSO	0.0519	0.00015	0.9934	2.608
ZCS@1.5CSO	0.0442	0.000147	0.9950	2.197

Tables 2 and 3 displayed the photocatalytic degradation performance and hydrogen evolution performance of MB for recent catalysts, respectively. Through comparing the results of photocatalytic degradation capabilities and the hydrogen evolution production rate constants, it was found that the photocatalytic degradation performance of the ZCS@1CSO composite material in this work was better among these photocatalysts. Additionally, the hydrogen evolution capability was above the middle level.

Table 2. The photocatalytic degradation performance of MB for recent catalysts.

Catalysts	Light Source	Concentration (mg/L)	Dosage (mg/mL)	C_t/C_0 at 40 min	Reference
copper oxide nanoparticle	sunlight	5	2	0.917	[56]
Poly(1-Napthylamine) nanoparticles	11 W UV irradiation	5	0.25	0.83	[57]
C_3N_5 nanosheet with Ag_2CO_3	300 W Xe light	60	1	0.28	[58]
ZnO-nanoparticles	sunlight	10	0.5	0.87	[59]
(Mn/TiO_2-WACF)	300 W Xe light	33	0.1	0.63	[60]
$SrTiO_3$ nanocube-doped polyaniline nanocomposites	300 W Xe light	10	0.3	0.29	[61]
Zn(II) coordination polymers	350 W Xe light	12.8	0.4	0.38	[62]
chitosan-modified nickel magnetite	sunlight	50	16.7	0.58	[63]
silver and graphene nanocomposites	500 W Xe light	3	0.4	0.7	[64]
ZCS@1CSO	300 W Xe light	10	0.667	0.031	this work

Table 3. The hydrogen evolution performance of recent catalysts.

Catalysts	Light Source	Apparent H_2 Production Rate Constant $(mmol \cdot g^{-1} \cdot h^{-1})$	Reference
$LaMnO_3$-Pt	300 W Xe light	1.350	[65]
thiophene-amide embedded g-C_3N_4	300 W Xe light	0.2454	[66]
g-C_3N_4/MoO_2 composites	300 W Xe light	0.3208	[67]
cds-ZTO	250 W metal-halide Philips lamp	0.548	[68]
RhCrOx/Pr-$LaFeO_3$	300 W Xe light	0.127	[69]
Ni/NiO/g-C_3N_4	300 W Xe light	2.310	[70]
ZnCdS/Co@CoO	300 W Xe light	5.445	[71]
UiO-66(Ce)/ZnCdS	300 W Xe light	3.958	[72]
Rod-shell CdS/Cu_2S	300 W Xe light	0.640	[21]
ZCS@1CSO	300 W Xe light	3.087	this work

The stability of photocatalytic materials was also very important for their further practical application. Figures 10c and S6 showed the experimental results of the ZCS@1CSO photocatalyst after four times of recycling. It could be seen that during the four times of usage, the efficiency of photocatalytic degradation of MB and hydrogen evolution with ZCS@1CSO was slightly decreased. However, the hydrogen production amount of 4 h was still maintained at 11.04 mmol·g^{-1}, and the residual rate of MB after 40 min reaction still reached 22%. Hence, the composite photocatalyst of ZCS@1CSO still kept about 80% of photocatalytic capacity after the fourth recycle. Moreover, Figure 10a,b depicted the SEM and XRD analysis results of the ZCS@1CSO photocatalyst after its fourth run. It could be seen from the XRD results that the positions and relative intensities of the characteristic peaks remained basically stable, which indicated that the composite material still contained abundant ZCS and CSO particles. Meanwhile, in Figure 10a, the larger CSO particles and nano ZCS particles supported on their surface could still be observed. However, compared with the original composite of ZCS@1CSO (Figure 4), the coverage of nano ZCS particles decreased. The results indicated that nano ZCS particles would fall off from the CSO surface during the photocatalysis experiment, which might be one of the reasons for the decline of photocatalytic ability after multiple usages.
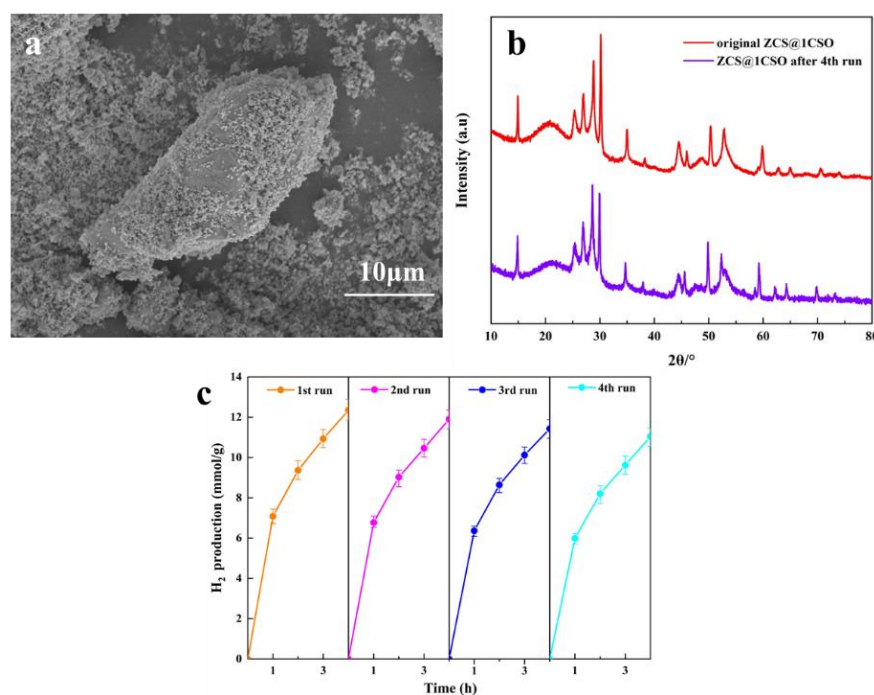

Figure 10. The SEM (**a**) and XRD (**b**) analysis results of ZCS@1CSO after its fourth run and H$_2$ production efficiency under the ZCS@1CSO photocatalytic system for four runs (**c**).

3.6. The Photocatalysis Mechanism

The electrochemical experiments, including transient photocurrent responses, electro-chemical impedance spectra, and Mott–Schottky curves, were very helpful to study the photocatalysis mechanism. Figure 11 showed the results of the transient photocurrent responses, electro-chemical impedance spectra, and Mott–Schottky curves of ZCS, CSO, and ZCS/1CSO catalytic materials. The results of Figure 11a suggested that all three materials displayed superior photocurrent responses, and the photocurrent response intensity of the ZCS/1CSO photocatalyst was the highest. It could also be seen in Figure S7a that the photocurrent response intensity of the ZCS/1CSO photocatalyst was higher than those of other heterojunction composite photocatalysts with different mass proportions. Such findings indicated that, through the recombination of ZCS and CSO materials, there would be more charge carriers in the composite samples under the optical excitation, which was

very helpful for the photocatalytic process. In addition, it could be seen in Figure 11b that, all three curves conformed to the classical semicircle shape, and their data could be fitted by inserting a circuit picture. As the order of the curve radius was ZCS/1CSO > ZCS > CSO, the ZCS/1CSO photocatalyst obtained the smallest charge transfer resistance, which was also conducive to the photocatalysis reaction. Meanwhile, Figure S7b suggested that among the composite photocatalysts with different composition ratios, the electrochemical impedance of ZCS/1CSO was the smallest. Additionally, according to the Mott–Schottky curve, it could be roughly known the type of semiconductor and the energy band range of the materials [73]. Because the slope of the fitting line was positive and the intercept to the *x*-axis was about −0.37 V, the ZCS was an n-type semiconductor and the flat band potential (E_{FB}) was −0.37 V. As we know, the E_{FB} of n-type semiconductor was about 0.2 V more positive than the conduction band potential (E_{CB}), so the E_{CB} of ZCS should be −0.57 V and the energy band range was from about −0.57 V to 1.88 V. Through the similar analysis methods, it was found that the CSO material was a p-type semiconductor and the energy band range was from about −0.6 V to 1.4 V. Moreover, in Figure 11e, an inverted "V" shape M–S curve could be observed, and both the parts similar to the curves of pure ZCS and CSO materials could be found. On the other hand, the slope of the fitting line was negatively correlated with the charge carrier density. The slope of the two fitting lines in Figure 11e was much lower than that of Figure 11c,d, and the charge carrier density of the ZCS@1CSO photocatalyst was much higher than that of the ZCS and CSO materials. In conclusion, these electrochemical experiments results indicated that the ZCS/1CSO composite should be a p-n type of heterojunction structure photocatalyst composed of ZCS and CSO materials, and the ZCS/1CSO composite photocatalyst exhibited excellent photocurrent response, lower impedance, and higher carrier density.

Meanwhile, according to the semiconductors physics knowledge [38], when the n-type semiconductors and p-type semiconductors were in contact, electrons and holes will undergo an interesting transfer between them due to their different types and positions of Fermi levels. As the results of the Mott–Schottky curves show, the band gap of the n-type ZCS ranged from about −0.57 V to 1.88 V, and the Fermi level was close to the conduction band, as shown in Figure 12a. Additionally, the band gap of the p-type CSO ranged from about −0.6 V to 1.4 V, and the Fermi level was close to the valence band and is also shown in Figure 12a. Additionally, near the contact surface of materials, the electrons would transfer from ZCS to CSO (while the moving of holes was in the opposite direction), thus causing the Fermi level of ZCS decrease and the one CSO increase. Finally, as shown in Figure 12b, the Fermi levels of two materials would reach the same position at the same time. Moreover, due to the interface movement of electrons and holes between the material of ZCS and CSO, an internal electric field (pointing from the ZCS to CSO material) would be formed. In this situation, when the composite material was excited by the visible light, electrons would be excited from the valence to the conduction bands and stay holes in the valence band in both ZCS and CSO materials. At this time, the established internal electric field would promote the transferring of photo-generated electrons from CSO to ZCS (holes transferring through the reverse direction). Such different transferring directions would greatly reduce the recombination probability of photo-generated holes and electrons, thus improving the photochemical activity of the compound photocatalytic material. Furthermore, this was consistent with the results of higher photocurrent, charge carrier density, and lower electrochemical impedance. In addition, after repeated uses, a small part of nano ZCS particles would fall off from the surface of the CSO material. Then, the transfer effect of photo-generated electrons and holes between ZCS and CSO materials was bound to be weakened, which led to the decline of its photocatalytic ability.
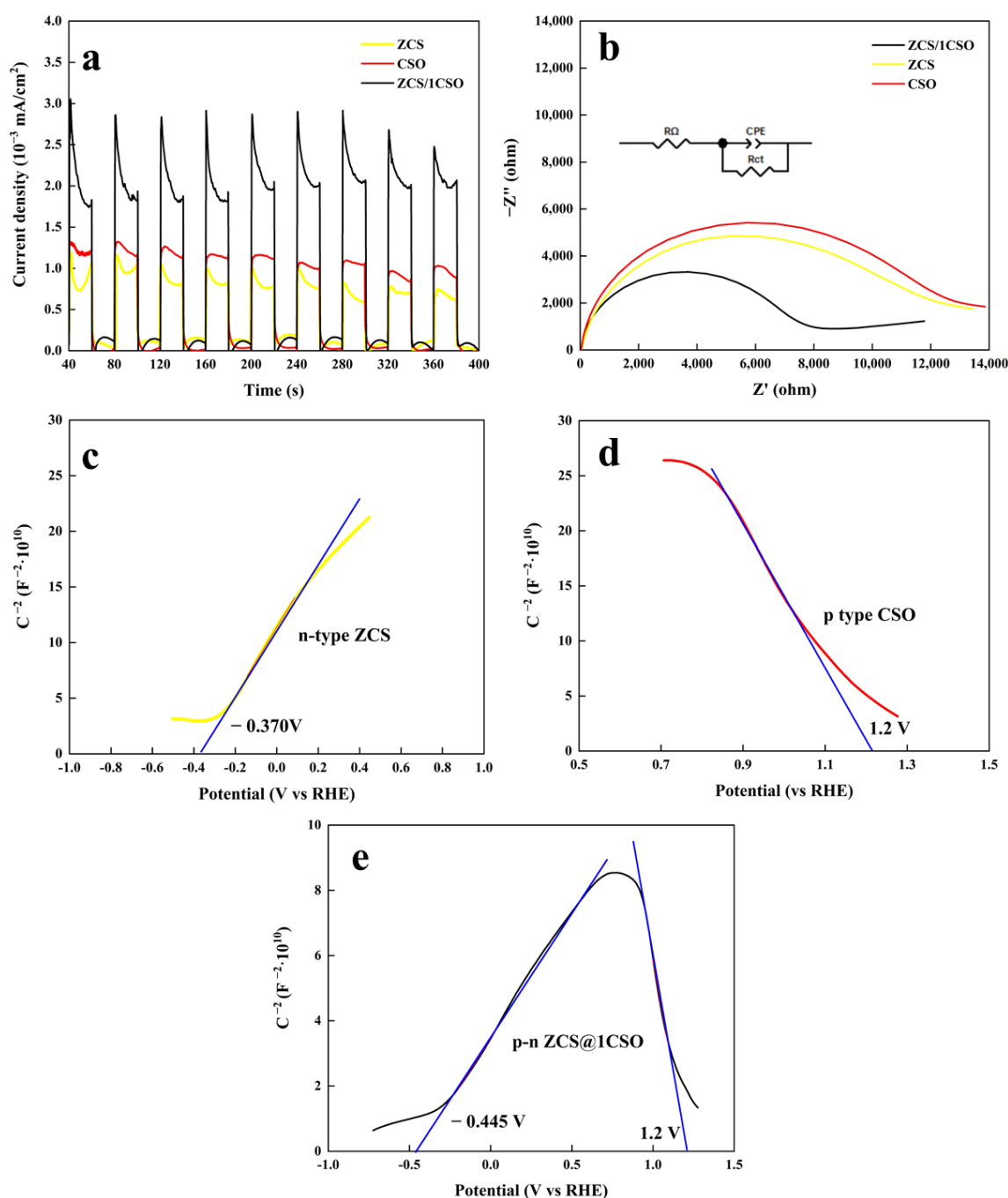
Figure 11. The transient photocurrent responses (**a**), Electro-chemical impedance spectra (**b**) and Mott–Schottky curves (**c–e**) of ZCS, CSO, and ZCS/1CSO.

The various free radicals, including photo-generated electrons (e^-), holes (h^+), superoxide radicals (O_2^-), and hydroxyl radicals (OH) in a photocatalysis system usually played important roles in the process of photocatalytic reaction. The ESR technology could detect many free radicals in the photocatalytic reaction, and the results of ESR spectra of ZCS@1CSO under dark and visible light were depicted in Figure 13. It could be seen in Figure 13a,b that after 5 min of irradiation with visible light, the signal of TEMPO was decreased significantly compared with 0 min (dark), since the decreasingsignal was caused by the combination of TEMPO and charge carriers (e^- and h^+) into other substances [74,75]. The results in Figure 13a,b suggested that some charge carriers (e^- and h^+) were generated by the radiation of visible light. Meanwhile, Figure 13c,d showed the detection results

of superoxide radicals and hydroxyl radicals. Compared with 0 min (dark), the signals of superoxide and hydroxyl radicals obviously appeared in Figure 13c,d after 5 min of irradiation with visible light. Because the detected signals belonged to complexes of DMOP and O_2^-/h$^+$ [76,77], these findings in Figure 13c,d indicated that some superoxide and hydroxyl radicals must be formed during the radiation of visible light.
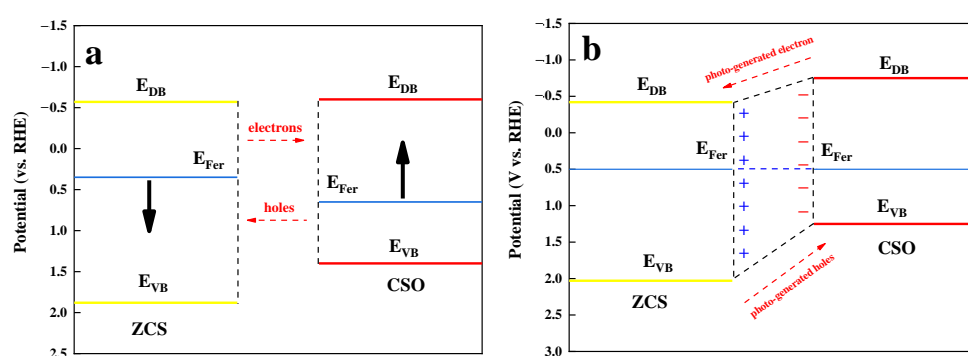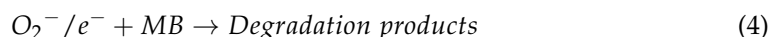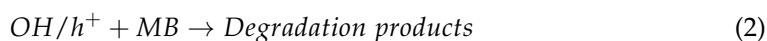
$$H_2O/OH^- + h^+ \rightarrow OH \tag{1}$$

$$OH/h^+ + MB \rightarrow Degradation\ products \tag{2}$$

$$O_2 + e^- \rightarrow O_2^- \tag{3}$$

$$O_2^-/e^- + MB \rightarrow Degradation\ products \tag{4}$$

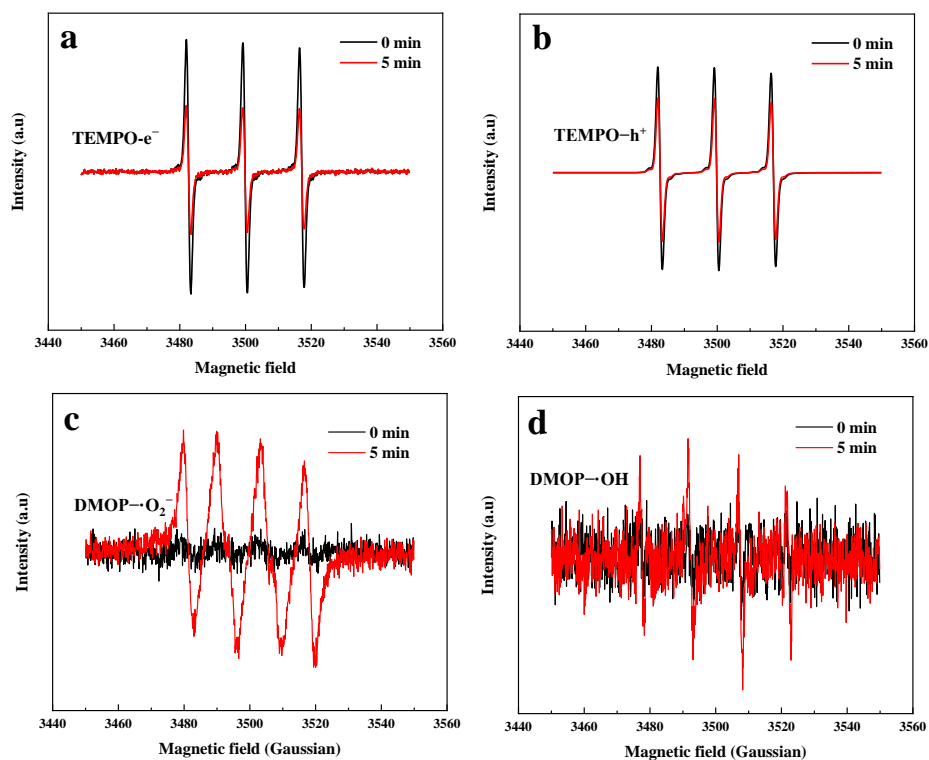**Figure 12.** The band gap structure of original ZCS and CSO (**a**), and a composite of ZCS and CSO (**b**).

Figure 13. The ESR spectra of ZCS/1CSO under dark (0 min) and visible light (5 min), (**a**): TEMPO-e$^-$, (**b**): TEMPO-h$^+$, (**c**): DMOP-O$_2^-$ and (**d**): DMOP-OH.

In addition to ESR technology, adding trapping agents was also one of the effective approaches to detect free radicals in the process of photocatalytic reaction. Figure 14 illustrated the influence of various trapping agents on the degradation process of MB. As we know, chemicals of EDTA-2Na, TBA, CCl_4, and BQ were trapping agents for the photogenerated hole, hydroxyl radical, electron, and superoxide radical, respectively [78,79]. It could be seen in Figure 14 that the photodegradation efficiencies of MB were decreased after the addition of four free radical trapping agents. This result implied that all four main free radicals, including e^-, h^+, OH, and O_2^-, must appear in the reaction process of photocatalysis, which was consistent with the results in Figure 13. For the degradation of MB, all the degradation reactions in Equations (1) to (4) would probably happen. Meanwhile, among the four trapping agents, the effects of CCl_4 and BQ in the degradation process were significantly higher than the others of EDTA-2Na and TBA. Hence, Equations (3) and (4) might be the main photodegradation path for MB in the photocatalytic reaction with composite photocatalysts. Meanwhile, the abundant photo-generated electrons could significantly reduce hydrogen ions in solution to hydrogen.
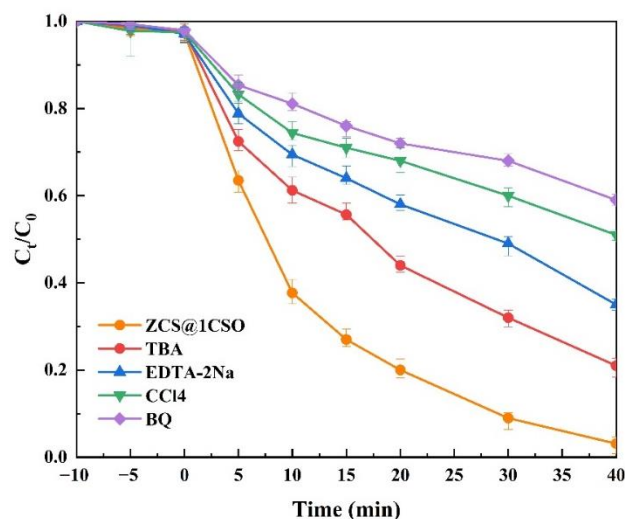

Figure 14. The influence of various trapping agents on the degradation process of MB.

Based on the results of photo-electrochemical properties and free radical detection, the photocatalytic mechanism of the composite materials could be simply summarized in Figure 15. It was revealed that the combination of two different semiconductor photocatalytic materials (the n-type of ZCS and the p-type of CSO) was beneficial to the separation of photo-generated charges and holes. When the ZCS and CSO materials were excited by the visible light, the photo-generated electrons in the conduction band of the CSO catalyst were transferred to ZCS, and the photo-generated holes in the valence band of ZCS were transferred to CSO. Then, the electrons concentrated in the conduction band of ZCS would directly reduce, or generate superoxide radicals to degrade the pollutant. At the same time, when the conditions were suitable, the hydrogen ions in the reaction system could also be reduced to hydrogen. Similarly, the holes concentrated in the valence band of CSO also could directly oxidize, or generate hydroxyl radicals to degrade the pollutant of MB. In this case, the efficient transferring of photo-generated electrons and holes was essential for the improvement of overall photocatalytic efficiency.
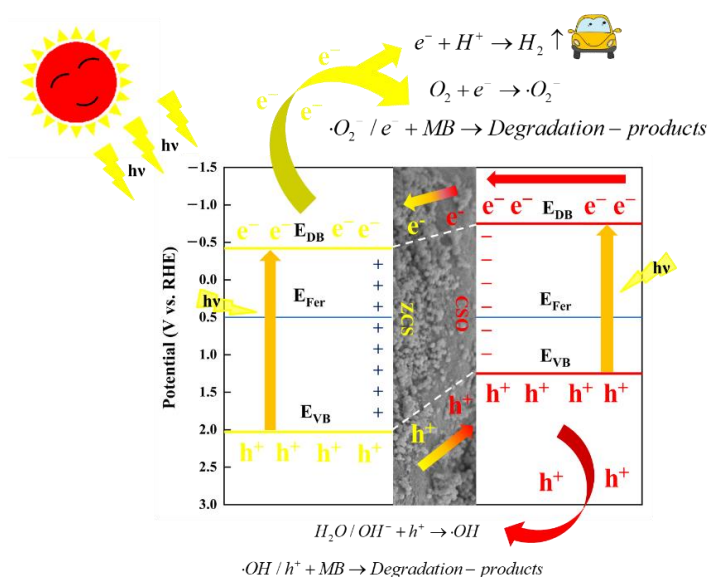
$$e^- + H^+ \rightarrow H_2 \uparrow$$

$$O_2 + e^- \rightarrow \cdot O_2^-$$

$$\cdot O_2^- / e^- + MB \rightarrow Degradation - products$$

$$H_2O / OH^- + h^+ \rightarrow \cdot OH$$

$$\cdot OH / h^+ + MB \rightarrow Degradation - products$$

Figure 15. The photocatalytic mechanism diagram of the ZCS and CSO composite photocatalyst.

4. Conclusions

In summary, novel composite photocatalysts of cobalt antimony oxide (CSO) and $Zn_{0.4}Cd_{0.6}S$ (ZCS) with different ratios were prepared and successfully synthesized by the hydrothermal reactions for the first time. The characterization results demonstrated that the heterojunction structure of synthesized composite materials was formed through the close adhesion of nano ZCS particles (about 100 nm) to the surface of larger CSO particles. The photocatalytic experiments verified that the composite photocatalysts could effectively enhance the photocatalytic degradation efficiencies of MB compared with those of single CSO, single ZCS, and other systems with the radiation of visible light. Meanwhile, the capability of hydrogen evolution reaction is also highly improved via the addition of composite photocatalysts. Among samples of photocatalysts with different proportions of CSO and ZCS, the photocatalyst of ZCS/1CSO exhibited optimal performance. The pseudo-first-order kinetic equation better described the degradation process of MB in different photocatalytic reaction systems. After being recycled four times, the photocatalyst could still maintain favorable stability in the photocatalytic reaction. The findings of electrochemical experiments proved that the transferring of photo-generated electrons and photo-generated holes between the n-type of ZCS and the p-type of CSO gave composite photocatalysts wider absorption for visible light, a stronger photo-current response, and a lower electrochemical impedance, which attributed to excellent photodegradation efficiencies of MB and hydrogen evolution abilities in the photocatalytic reaction. The MB could be completely photodegraded in 40 min, and the apparent hydrogen production rate was about 3.087 mmol·g^{-1}·h^{-1}. Moreover, the photocatalytic mechanism revealed that four types of highly active substances, including photo-generated electrons, photo-generated holes, superoxide radicals, and hydroxyl radicals, contributed to the photocatalytic degradation of MB. Additionally, the photo-generated electrons and superoxide radicals played crucial roles in the photodegradation of the target pollutant. Furthermore, the photo-generated electrons concentrated in the conduction band of ZCS should be conducive to the improvement of hydrogen evolution ability for composite photocatalysts. The results in this paper could be applied in the photocatalytic treatment of dye wastewater and hydrogen evolution-based new energy. In future research, we will further study the catalytic mechanism to find a more efficient photocatalysis process.

Supplementary Materials: The following are available online at https://www.mdpi.com/article/10.3390/w14233827/s1, Figure S1: XRD patterns of ZCS/CSO heterojunction with different mass ratio (Z: ZCS and C: CSO), Figure S2: UV-Vis diffuse reflectance spectra for ZCS/CSO heterojunction with different mass ratio (a), and the plotting results of band gaps energy for ZCS/CSO heterojunction with different mass ratio (b), Figure S3: The SEM analysis results of ZCS (a and b) and EDS mapping results of Cd (c), Zn (d) and S (e), Figure S4: The wide scan XPS of ZCS (a); the high-resolution XPS spectra of Cd3d (b), Zn2p (c) and S2p (d), Figure S5: The MB photocatalytic degradation process (a), kinetic analysis (b) and H_2 production (c) under composite systems (with different ZCS and CSO ratios), Figure S6: The MB photocatalytic degradation efficiency under ZCS@1CSO system for four runs, Figure S7: The transient photocurrent responses (a), Electro-chemical impedance spectra (b) for ZCS/CSO heterojunction with different mass ratio.

Author Contributions: C.C. and X.Z. created the original study plan; T.C. and M.W. designed and executed the experiments under the guidance of X.Z. and C.C.; C.C. wrote the manuscript; Y.T. and B.H. reviewed and edited the manuscript. All authors have read and agreed to the published version of the manuscript.

Data Availability Statement: Not applicable.

Conflicts of Interest: The authors declare no conflict of interest.

References

1. Li, L.; Shi, Y.; Huang, Y.; Xing, A.; Xue, H. The Effect of Governance on Industrial Wastewater Pollution in China. *Int. J. Environ. Res. Public Health* **2022**, *19*, 9316. [CrossRef] [PubMed]
2. Tang, W.; Pei, Y.; Zheng, H.; Zhao, Y.; Shu, L.; Zhang, H. Twenty years of China's water pollution control: Experiences and challenges. *Chemosphere* **2022**, *295*, 133875. [CrossRef] [PubMed]
3. Jia, Z.; Lin, B. How to achieve the first step of the carbon-neutrality 2060 target in China: The coal substitution perspective. *Energy* **2021**, *233*, 121179. [CrossRef]
4. Li, Y.; Yang, X.; Ran, Q.; Wu, H.; Irfan, M.; Ahmad, M. Energy structure, digital economy, and carbon emissions: Evidence from China. *Environ. Sci. Pollut. Res.* **2021**, *28*, 64606–64629. [CrossRef]
5. Bhat, A.H.; Rangreez, T.A.; Inamuddin; Chisti, H.-T.-N. Wastewater Treatment and Biomedical Applications of Montmorillonite Based Nanocomposites: A Review. *Curr. Anal. Chem.* **2022**, *18*, 269–287. [CrossRef]
6. Morin-Crini, N.; Lichtfouse, E.; Fourmentin, M.; Ribeiro, A.R.L.; Noutsopoulos, C.; Mapelli, F.; Fenyvesi, E.; Vieira, M.G.A.; Picos-Corrales, L.A.; Moreno-Pirajan, J.C.; et al. Removal of emerging contaminants from wastewater using advanced treatments. A review. *Environ. Chem. Lett.* **2022**, *20*, 1333–1375. [CrossRef]
7. Wang, B.W.; Wang, Y. A comprehensive review on persulfate activation treatment of wastewater. *Sci. Total Environ.* **2022**, *831*, 154906. [CrossRef]
8. Garcia-Segura, S.; Ocon, J.D.; Chong, M.N. Electrochemical oxidation remediation of real wastewater effluents—A review. *Process Saf. Environ. Prot.* **2018**, *113*, 48–67. [CrossRef]
9. Kasonga, T.K.; Coetzee, M.A.A.; Kamika, I.; Ngole-Jeme, V.M.; Momba, M.N.B. Endocrine-disruptive chemicals as contaminants of emerging concern in wastewater and surface water: A review. *J. Environ. Manag.* **2021**, *277*, 111485. [CrossRef]
10. Schneider, S.L.; Lim, H.W. Review of environmental effects of oxybenzone and other sunscreen active ingredients. *J. Am. Acad. Dermatol.* **2019**, *80*, 266–271. [CrossRef]
11. Alabi, O.A. Comparative chemical analysis, mutagenicity, and genotoxicity of Petroleum refinery wastewater and its contaminated river using prokaryotic and eukaryotic assays. *Protoplasma* **2022**, 1–13. [CrossRef] [PubMed]
12. Xue, P.; Zhao, Y.; Zhao, D.; Chi, M.; Yin, Y.; Xuan, Y.; Wang, X. Mutagenicity, health risk, and disease burden of exposure to organic micropollutants in water from a drinking water treatment plant in the Yangtze River Delta, China. *Ecotoxicol. Environ. Saf.* **2021**, *221*, 112421. [CrossRef] [PubMed]
13. Jirova, G.; Wittlingerova, Z.; Zimova, M.; Vlkova, A.; Wittlerova, M.; Dvorakova, M.; Jirova, D. Bioindicators of wastewater ecotoxicity. *Neuroendocrinol. Lett.* **2016**, *37*, 17–24. [PubMed]
14. Koopaei, N.N.; Abdollahi, M. Health risks associated with the pharmaceuticals in wastewater. *Daru-J. Pharm. Sci.* **2017**, *25*, 9. [CrossRef] [PubMed]
15. Lin, S.-S.; Shen, S.-L.; Zhou, A.; Lyu, H.-M. Assessment andmanagement of lake eutrophication: A case study in Lake Erhai, China. *Sci. Total Environ.* **2021**, *751*, 141618. [CrossRef]
16. Preisner, M.; Neverova-Dziopak, E.; Kowalewski, Z. Analysis of eutrophication potential of municipal wastewater. *Water Sci. Technol.* **2020**, *81*, 1994–2003. [CrossRef]

17.　Panagopoulos, A. Brine management (saline water & wastewater effluents): Sustainable utilization and resource recovery strategy through Minimal and Zero Liquid Discharge (MLD & ZLD) desalination systems. *Chem. Eng. Process. Process Intensif.* **2022**, *176*, 108944. [CrossRef]

18.　Panagopoulos, A.; Giannika, V. Decarbonized and circular brine management/valorization for water & valuable resource recovery via minimal/zero liquid discharge (MLD/ZLD) strategies. *J. Environ. Manag.* **2022**, *324*, 116239. [CrossRef]

19.　Panagopoulos, A. Process simulation and analysis of high-pressure reverse osmosis (HPRO) in the treatment and utilization of desalination brine (saline wastewater). *Int. J. Energy Res.* **2022**. [CrossRef]

20.　Chen, C.X.; Xiong, Y.Y.; Zhong, X.; Lan, P.C.; Wei, Z.W.; Pan, H.; Su, P.Y.; Song, Y.; Chen, Y.F.; Nafady, A.; et al. Enhancing Photocatalytic Hydrogen Production via the Construction of Robust Multivariate Ti-MOF/COF Composites. *Angew. Chem. Int. Ed.* **2022**, *61*, e202114071. [CrossRef]

21.　Guo, Y.; Liang, Z.; Xue, Y.; Wang, X.; Zhang, X.; Tian, J. A cation exchange strategy to construct Rod-shell CdS/Cu$_2$S nanostructures for broad spectrum photocatalytic hydrogen production. *J. Colloid Interface Sci.* **2022**, *608*, 158–163. [CrossRef] [PubMed]

22.　Liang, Z.; Shen, R.; Ng, Y.H.; Zhang, P.; Xiang, Q.; Li, X. A review on 2D MoS$_2$ cocatalysts in photocatalytic H-2 production. *J. Mater. Sci. Technol.* **2020**, *56*, 89–121. [CrossRef]

23.　Chen, D.; Cheng, Y.; Zhou, N.; Chen, P.; Wang, Y.; Li, K.; Huo, S.; Cheng, P.; Peng, P.; Zhang, R.; et al. Photocatalytic degradation of organic pollutants using TiO2-based photocatalysts: A review. *J. Clean. Prod.* **2020**, *268*, 121725. [CrossRef]

24.　Liu, Z.; Yu, Y.; Zhu, X.; Fang, J.; Xu, W.; Hu, X.; Li, R.; Yao, L.; Qin, J.; Fang, Z. Semiconductor heterojunctions for photocatalytic hydrogen production and Cr(VI) Reduction: A review. *Mater. Res. Bull.* **2022**, *147*, 111636. [CrossRef]

25.　Cheung, K.P.S.; Sarkar, S.; Gevorgyan, V. Visible Light-Induced Transition Metal Catalysis. *Chem. Rev.* **2022**, *122*, 1543–1625. [CrossRef]

26.　Gao, C.; Low, J.; Long, R.; Kong, T.; Zhu, J.; Xiong, Y. Heterogeneous Single-Atom Photocatalysts: Fundamentals and Applications. *Chem. Rev.* **2020**, *120*, 12175–12216. [CrossRef]

27.　Jin, P.; Wang, L.; Ma, X.; Lian, R.; Huang, J.; She, H.; Zhang, M.; Wang, Q. Construction of hierarchical ZnIn$_2$S$_4$@PCN-224 heterojunction for boosting photocatalytic performance in hydrogen production and degradation of tetracycline hydrochloride. *Appl. Catal. B-Environ.* **2021**, *284*, 119762. [CrossRef]

28.　Chen, C.; Cheng, T.; Wang, L.; Xu, Y.; Zhang, X. Surface functionalization of Linde F (K) nano-zeolite and its application for photocatalytic wastewater treatment and hydrogen production. *Appl. Phys. A* **2022**, *128*, 468. [CrossRef]

29.　Juárez-Cortazar, D.E.; Torres-Torres, J.G.; Hernandez-Ramirez, A.; Arévalo-Pérez, J.C.; Cervantes-Uribe, A.; Godavarthi, S.; de los Monteros, A.E.E.; Silahua-Pavón, A.A.; Cordero-Garcia, A. Doping of TiO2 Using Metal Waste (Door Key) to Improve Its Photocatalytic Efficiency in the Mineralization of an Emerging Contaminant in an Aqueous Environment. *Water* **2022**, *14*, 1389. [CrossRef]

30.　Park, Y.; Kim, S.; Kim, J.; Khan, S.; Han, C. UV/TiO2 Photocatalysis as an Efficient Livestock Wastewater Quaternary Treatment for Antibiotics Removal. *Water* **2022**, *14*, 958. [CrossRef]

31.　Asadzadeh-Khaneghah, S.; Habibi-Yangjeh, A. g-C$_3$N$_4$/carbon dot-based nanocomposites serve as efficacious photocatalysts for environmental purification and energy generation: A review. *J. Clean. Prod.* **2020**, *276*, 124319. [CrossRef]

32.　He, F.; Zhu, B.; Cheng, B.; Yu, J.; Ho, W.; Macyk, W. 2D/2D/0D TiO$_2$/C$_3$N$_4$/Ti$_3$C$_2$ MXene composite S-scheme photocatalyst with enhanced CO$_2$ reduction activity. *Appl. Catal. B-Environ.* **2020**, *272*, 119006. [CrossRef]

33.　Smazna, D.; Shree, S.; Polonskyi, O.; Lamaka, S.; Baum, M.; Zheludkevich, M.; Faupel, F.; Adelung, R.; Mishra, Y.K. Mutual interplay of ZnO micro- and nanowires and methylene blue during cyclic photocatalysis process. *J. Environ. Chem. Eng.* **2019**, *7*, 103016. [CrossRef]

34.　Pan, L.; Muhammad, T.; Ma, L.; Huang, Z.-F.; Wang, S.; Wang, L.; Zou, J.-J.; Zhang, X. MOF-derived C-doped ZnO prepared via a two-step calcination for efficient photocatalysis. *Appl. Catal. B-Environ.* **2016**, *189*, 181–191. [CrossRef]

35.　Sun, B.; Liang, Z.; Qian, Y.; Xu, X.; Han, Y.; Tian, J. Sulfur Vacancy-Rich O-Doped 1T-MoS$_2$ Nanosheets for Exceptional Photocatalytic Nitrogen Fixation over CdS. *ACS Appl. Mater. Interfaces* **2020**, *12*, 7257–7269. [CrossRef]

36.　Wang, L.; Xie, L.; Zhao, W.; Liu, S.; Zhao, Q. Oxygen-facilitated dynamic active-site generation on strained MoS$_2$ during photo-catalytic hydrogen evolution. *Chem. Eng. J.* **2021**, *405*, 127028. [CrossRef]

37.　Liu, Q.; Fan, C.; Liu, J.; Sun, X.; Cheng, X.; Li, H. Synthesis, photocatalytic performance and negative thermal expansion property of nanorods ZrMo$_{2−x}$ V$_{(x)}$ O$_{8-x/2}$ with cubic structure. *J. Sol-Gel Sci. Technol.* **2015**, *76*, 279–288. [CrossRef]

38.　Chen, C.; Wen, M.; Cheng, T.; Wang, L.; Zhang, X.; Tian, Y. Photocatalytic degradation of tetracycline wastewater through heterojunction based on 2D rhombic ZrMo$_2$O$_8$ nanosheet and nano-TiO$_2$. *J. Nanoparticle Res.* **2022**, *24*, 172. [CrossRef]

39.　Yin, H.; Cao, Y.; Fan, T.; Zhang, M.; Yao, J.; Li, P.; Chen, S.; Liu, X. In situ synthesis of Ag$_3$PO$_4$/C$_3$N$_5$ Z-scheme heterojunctions with enhanced visible-light-responsive photocatalytic performance for antibiotics removal. *Sci. Total Environ.* **2021**, *754*, 141926. [CrossRef]

40.　Mu, F.; Dai, B.; Zhao, W.; Zhou, S.; Huang, H.; Yang, G.; Xia, D.; Kong, Y.; Leung, D.Y.C. Construction of a novel Ag/Ag$_3$ PO$_4$/MIL-68(In)-NH$_2$ plasmonic heterojunction photocatalyst for high-efficiency photocatalysis. *J. Mater. Sci. Technol.* **2022**, *101*, 37–48. [CrossRef]

41.　Chen, C.; Wang, L.; Cheng, T.; Zhang, X.; Zhou, Z.; Zhang, X.; Xu, Q. Ag$_3$PO$_4$/Ag$_{Sb}$O$_3$ composite as novel photocatalyst with significantly enhanced activity through a Z-scheme degradation mechanism. *J. Iran. Chem. Soc.* **2022**, *19*, 821–838. [CrossRef]

42. Liu, Y.; Zheng, X.; Yang, Y.; Song, Y.; Yang, Y.; Li, J.; Shim, C.M.; Shen, Y.; Tian, X. Recent Advances in the Hydrogen Evolution Reaction of ZnxCd1-xS-Based Photocatalysts. *Sol. RRL* **2022**, *6*, 2101061. [CrossRef]

43. Madhusudan, P.; Shi, R.; Xiang, S.; Jin, M.; Chandrashekar, B.N.; Wang, J.; Wang, W.; Peng, O.; Amini, A.; Cheng, C. Construction of highly efficient Z-scheme $Zn_xCd_{1-x}S/Au@g-C_3N_4$ ternary heterojunction composite for visible-light-driven photocatalytic reduction of CO_2 to solar fuel. *Appl. Catal. B-Environ.* **2021**, *282*, 119600. [CrossRef]

44. Shen, R.C.; Ding, Y.N.; Li, S.B.; Zhang, P.; Xiang, Q.J.; Ng, Y.H.; Li, X. Constructing low-cost Ni_3C/twin-crystal $Zn_{0.5}Cd_{0.5}S$ heterojunction/homojunction nanohybrids for efficient photocatalytic H-2 evolution. *Chin. J. Catal.* **2021**, *42*, 25–36. [CrossRef]

45. Ge, G.Y.; Yuan, S.T.; Liu, Q.Z.; Yang, D.F.; Shi, J.S.; Lan, X.F.; Xiao, K.F. Insight into the function of noble-metal free Cu_3P decorated $Zn_{0.5}Cd_{0.5}S$ for enhanced photocatalytic hydrogen evolution under visible light irradiation- mechanism for continuous increasing activity. *Appl. Surf. Sci.* **2022**, *597*, 153660. [CrossRef]

46. Liu, H.; Zhang, Y.Y.; Li, D.J.; Li, Y.J.; Jin, Z.L. Design and Preparation of a $CeVO_4/Zn_{0.5}Cd_{0.5}S$ S-Scheme Heterojunction for Efficient Photocatalytic Hydrogen Evolution. *ACS Appl. Energy Mater.* **2022**, *5*, 2474–2483. [CrossRef]

47. Qi, S.Y.; Zhang, K.Y.; Zhang, Y.M.; Zhang, R.Y.; Xu, H.Y. Synthesis of $WS_2/Zn_{0.5}Cd_{0.5}S$ Nanoheterostructured Photocatalyst and Its Visible Light Catalytic Performance. *J. Inorg. Organomet. Polym. Mater.* **2022**, *32*, 3923–3931. [CrossRef]

48. Duo, J.; Li, W.; Wang, Y.; Wang, S.; Wufuer, R.; Pan, X. Photothermal Catalytic Degradation of Lomefloxacin with Nano Au/TiO_2. *Water* **2022**, *14*, 339. [CrossRef]

49. Chen, C.; Wang, L.; Cheng, T.; Zhang, X.; Tian, Y.; Shi, Y. Sliver Doped Sodium Antimonate with Greatly Reduced the Band Gap for Efficiently Enhanced Photocatalytic Activities Under Visible Light (Experiment and DFT Calculation). *Mater. Res.* **2021**, *24*, e20210100. [CrossRef]

50. Dai, D.; Xu, H.; Ge, L.; Han, C.; Gao, Y.; Li, S.; Lu, Y. In-situ synthesis of CoP co-catalyst decorated $Zn_{0.5}Cd_{0.5}S$ photocatalysts with enhanced photocatalytic hydrogen production activity under visible light irradiation. *Appl. Catal. B Environ.* **2017**, *217*, 429–436. [CrossRef]

51. Tang, Y.; Li, X.; Zhang, D.; Pu, X.; Ge, B.; Huang, Y. Noble metal-free ternary $MoS_2/Zn_{0.5}Cd_{0.5}S/g-C_3N_4$ heterojunction composite for highly efficient photocatalytic H_2 production. *Mater. Res. Bull.* **2019**, *110*, 214–222. [CrossRef]

52. Ham, K.; Hong, S.; Kang, S.; Cho, K.; Lee, J. Extensive Active-Site Formation in Trirutile $CoSb_2O_6$ by Oxygen Vacancy for Oxygen Evolution Reaction in Anion Exchange Membrane Water Splitting. *ACS Energy Lett.* **2021**, *6*, 364–370. [CrossRef]

53. Evans, T.A.; Choi, K.-S. Electrochemical Synthesis and Investigation of Stoichiometric, Phase-Pure $CoSb_2O_6$ and $MnSb_2O_6$ Electrodes for the Oxygen Evolution Reaction in Acidic Media. *ACS Appl. Energy Mater.* **2020**, *3*, 5563–5571. [CrossRef]

54. Zhang, X.; Cheng, T.; Chen, C.; Wang, L.; Deng, Q.; Chen, G.; Ye, C. Synthesis of a novel magnetic nano-zeolite and its application as an efficient heavy metal adsorbent. *Mater. Res. Express* **2020**, *7*, 085007. [CrossRef]

55. Nutescu Duduman, C.; Gómez de Castro, C.; Apostolescu, G.A.; Ciobanu, G.; Lutic, D.; Favier, L.; Harja, M. Enhancing the TiO_2-Ag Photocatalytic Efficiency by Acetone in the Dye Removal from Wastewater. *Water* **2022**, *14*, 2711. [CrossRef]

56. Yasin, A.; Fatima, U.; Shahid, S.; Mansoor, S.; Inam, H.; Javed, M.; Iqbal, S.; Alrbyawi, H.; Somaily, H.H.; Pashameah, R.A.; et al. Fabrication of Copper Oxide Nanoparticles Using Passiflora edulis Extract for the Estimation of Antioxidant Potential and Photocatalytic Methylene Blue Dye Degradation. *Agronomy* **2022**, *12*, 2315. [CrossRef]

57. Umar, A.; Kumar, S.A.; Rosaline, D.R.; Algadi, H.; Ibrahim, A.A.; Ahmed, F.; Foletto, E.L.; Inbanathan, S.S.R. Poly(1-Napthylamine) Nanoparticles as Potential Scaffold for Supercapacitor and Photocatalytic Applications. *Micromachines* **2022**, *13*, 1528. [CrossRef]

58. Li, G.; Zeng, G.; Chen, Z.; Hong, J.; Ji, X.; Lan, Z.; Tan, X.; Li, M.; Hu, X.; Tang, C. In Situ Coupling Carbon Defective C_3N_5 Nanosheet with Ag_2CO_3 for Effective Degradation of Methylene Blue and Tetracycline Hydrochloride. *Nanomaterials* **2022**, *12*, 2701. [CrossRef]

59. Dhatwalia, J.; Kumari, A.; Chauhan, A.; Mansi, K.; Thakur, S.; Saini, R.V.; Guleria, I.; Lal, S.; Kumar, A.; Batoo, K.M.; et al. Rubus ellipticus Sm. Fruit Extract Mediated Zinc Oxide Nanoparticles: A Green Approach for Dye Degradation and Biomedical Applications. *Materials* **2022**, *15*, 3470. [CrossRef]

60. Ma, X.; Zhou, W.; Chen, Y. Structure and Photocatalytic Properties of Mn-Doped TiO_2 Loaded on Wood-Based Activated Carbon Fiber Composites. *Materials* **2017**, *10*, 631. [CrossRef]

61. Shahabuddin, S.; Muhamad Sarih, N.; Mohamad, S.; Joon Ching, J. $SrTiO_3$ Nanocube-Doped Polyaniline Nanocomposites with Enhanced Photocatalytic Degradation of Methylene Blue under Visible Light. *Polymers* **2016**, *8*, 27. [CrossRef] [PubMed]

62. Liu, L.-L.; Yu, C.-X.; Zhou, W.; Zhang, Q.-G.; Liu, S.-M.; Shi, Y.-F. Construction of Four Zn(II) Coordination Polymers Used as Catalysts for the Photodegradation of Organic Dyes in Water. *Polymers* **2016**, *8*, 3. [CrossRef] [PubMed]

63. Ara, A.; Khattak, R.; Khan, M.S.; Begum, B.; Khan, S.; Han, C. Synthesis, Characterization, and Solar Photo-Activation of Chitosan-Modified Nickel Magnetite Bio-Composite for Degradation of Recalcitrant Organic Pollutants in Water. *Catalysts* **2022**, *12*, 983. [CrossRef]

64. Malik, S.B.; Saggu, J.I.; Gul, A.; Abbasi, B.A.; Iqbal, J.; Waris, S.; Jardan, Y.A.B.; Chalgham, W. Synthesis and Characterization of Silver and Graphene Nanocomposites and Their Antimicrobial and Photocatalytic Potentials. *Molecules* **2022**, *27*, 5184. [CrossRef]

65. Jawhari, A.H.; Hasan, N.; Radini, I.A.; Narasimharao, K.; Malik, M.A. Noble Metals Deposited $LaMnO_3$ Nanocomposites for Photocatalytic H_2 Production. *Nanomaterials* **2022**, *12*, 2985. [CrossRef]

66. Tang, S.; Xu, Y.-S.; Zhang, W.-D. Embedding Thiophene-Amide into $g-C_3N_4$ Skeleton with Induction and Delocalization Effects for High Photocatalytic H_2 Evolution. *Protoplasma* **2022**, *12*, 1043. [CrossRef]

67. Chen, Y.; Li, A.; Fu, X.; Peng, Z. One-Step Calcination to Gain Exfoliated g-C$_3$N$_4$/MoO$_2$ Composites for High-Performance Photocatalytic Hydrogen Evolution. *Molecules* **2022**, *27*, 7178. [CrossRef]

68. Pantoja-Espinoza, J.C.; Domínguez-Arvizu, J.L.; Jiménez-Miramontes, J.A.; Hernández-Majalca, B.C.; Meléndez-Zaragoza, M.J.; Salinas-Gutiérrez, J.M.; Herrera-Pérez, G.M.; Collins-Martínez, V.H.; López-Ortiz, A. Comparative Study of Zn$_2$Ti$_3$O$_8$ and ZnTiO$_3$ Photocatalytic Properties for Hydrogen Production. *Catalysts* **2020**, *10*, 1372. [CrossRef]

69. Chiang, T.H.; Viswanath, G.; Chen, Y.-S. Effects of RhCrOx Cocatalyst Loaded on Different Metal Doped LaFeO$_3$ Perovskites with Photocatalytic Hydrogen Performance under Visible Light Irradiation. *Catalysts* **2021**, *11*, 612. [CrossRef]

70. Zhang, T.; Liu, P.; Wang, L.; Wang, S.; Shi, J.; Lan, X. Electronegativity Assisted Synthesis of Magnetically Recyclable Ni/NiO/g-C$_3$N$_4$ for Significant Boosting H$_2$ Evolution. *Materials* **2021**, *14*, 2894. [CrossRef]

71. Zou, Y.; Guo, C.; Cao, X.; Chen, T.; Kou, Y.; Zhang, L.; Wang, T.; Akram, N.; Wang, J. Photocatalytic performance and mechanism of hydrogen evolution from water over ZnCdS/Co@CoO in sacrificial agent-free system. *Int. J. Hydrogen Energy* **2022**, *47*, 25289–25299. [CrossRef]

72. Wang, Y.; Jin, H.; Li, Y.; Fang, J.; Chen, C. Ce-based organic framework enhanced the hydrogen evolution ability of ZnCdS photocatalyst. *Int. J. Hydrogen Energy* **2022**, *47*, 962–970. [CrossRef]

73. Ji, Y.; Zhou, Y.; Wang, J.; Li, A.; Bian, W.; Corvini, P.F.-X. Au@CoS-BiVO$_4$ (010) Constructed for Visible-Light-Assisted Peroxy-monosulfate Activation. *Catalysts* **2021**, *11*, 1414. [CrossRef]

74. Gao, J.; Zhang, F.; Xue, H.; Zhang, L.; Peng, Y.; Li, X.; Gao, Y.; Li, N.; Lei, G. In-situ synthesis of novel ternary CdS/PdAg/g-C$_3$N$_4$ hybrid photocatalyst with significantly enhanced hydrogen production activity and catalytic mechanism exploration. *Appl. Catal. B Environ.* **2021**, *281*, 119509. [CrossRef]

75. Li, X.-L.; Yang, G.Q.; Li, S.S.; Xiao, N.; Li, N.; Gao, Y.Q.; Lv, D.; Ge, L. Novel dual co-catalysts decorated Au@HCS@PdS hybrids with spatially separated charge carriers and enhanced photocatalytic hydrogen evolution activity. *Chem. Eng. J.* **2020**, *379*, 122350. [CrossRef]

76. Zhu, H.; Ji, Y.; Chen, L.; Bian, W.; Wang, J. Pt Nanowire-Anchored Dodecahedral Ag$_3$PO$_4${110} Constructed for Significant Enhancement of Photocatalytic Activity and Anti-Photocorrosion Properties: Spatial Separation of Charge Carriers and Photogen-eratedElectron Utilization. *Catalysts* **2020**, *10*, 206. [CrossRef]

77. Huo, H.; Hu, X.; Wang, H.; Li, J.; Xie, G.; Tan, X.; Jin, Q.; Zhou, D.; Li, C.; Qiu, G.; et al. Synergy of Photocatalysis and Adsorption for Simultaneous Removal of Hexavalent Chromium and Methylene Blue by g-C$_3$N$_4$/BiFeO$_3$/Carbon Nanotubes Ternary Composites. *Int. J. Environ. Res. Public Health* **2019**, *16*, 3219. [CrossRef]

78. Chen, F.F.; Wu, C.Y.; Wang, J.N.; Francois-Xavier, C.P.; Wintgens, T. Highly efficient Z-scheme structured visible-light photocatalyst constructed by selective doping of Ag@AgBr and Co$_3$O$_4$ separately on {010} and {110} facets of BiVO4: Pre-separation channel and hole-sink effects. *Appl. Catal. B-Environ.* **2019**, *250*, 31–41. [CrossRef]

79. Liu, H.; Chen, H.; Ding, N. Visible Light-Based Ag$_3$PO$_4$/g-C$_3$N$_4$@MoS$_2$ for Highly Efficient Degradation of 2-Amino-4-acetylaminoanisole (AMA) from Printing and Dyeing Wastewater. *Int. J. Environ. Res. Public Health* **2022**, *19*, 2934. [CrossRef]